

Aeroacoustic Optimization of Flat-Plate Serrated Trailing Edge Extensions for Broadband Noise Reduction

by

Matthew A.J. Brezina

A thesis submitted to the Faculty of Graduate and Postdoctoral
Affairs in partial fulfillment of the requirements for the degree of

Master of Applied Science

in

Aerospace Engineering

Carleton University
Ottawa, Ontario

© 2016, Matthew A.J. Brezina

ABSTRACT

The ability of trailing edge serrations to reduce turbulent boundary layer trailing edge noise is examined through numerical optimization studies. The in-house optimization program, SAGRGSTEN, is developed and implemented. Two different serration geometries are optimized for both, the overall noise (from 20 Hz to 20 kHz), and the noise produced at individual frequencies throughout the same range. The noise was modeled using Howe's semi-empirical model for a semi-infinite flat plate, at zero angle of attack to the mean, low Mach number, flow. Results of the optimization studies are used to investigate the influence of serration design parameters. It is shown that the multi-tooth-size serrated trailing edges yield greater noise reductions than single-size serrated trailing edges. Based on this finding, a novel design is proposed for a multi-tooth-size sawtooth serrated TE profile. It is also shown that, based on the bounds used, the serration design that yields the greatest amount of total noise reduction is a multi-tooth-size slitted trailing edge.

To Rachel, thank you for always believing in me.

ACKNOWLEDGEMENTS

I offer my sincere gratitude to my supervisor, Professor Joana Rocha, whose time, resources, and patience have been greatly appreciated. Thank you for encouraging me to achieve more, always work harder, and maintain perspective.

I gratefully acknowledge the Mechanical and Aerospace Engineering Department at Carleton University for the financial support that made it possible to present my work at the 2016 ASA conference.

I would like to thank my friend and colleague Jared Van Blitterswyk. From welcoming me to Carleton and Ottawa to the insightful and motivating research discussions, his help and friendship made this work possible.

I would also like to thank my parents for their unconditional support throughout all of my endeavors. They have made it possible for me to, not only have dreams, but to achieve them as well. For everything they have done for me, I am truly grateful.

Finally, I would like to give a special thanks to Rachel Hurdle for being there in the toughest of times to help me through. I am so fortunate to have someone like her in my life. Her patience, understanding and kindness were the cornerstone to completing this work.

TABLE OF CONTENTS

Abstract.....	ii
Acknowledgements	iv
Table of Contents	v
List of Tables	viii
List of Figures.....	ix
List of Abbreviations	xii
Nomenclature	xiii
Chapter 1 Introduction.....	1
1.1 Motivation.....	1
1.2 Literature Review.....	4
1.2.1 Production of Trailing Edge Noise.....	4
1.2.2 Trailing Edge Serrations.....	7
1.2.3 Influence of Nature on Serration Design.....	10
1.2.4 Optimization for Trailing Edge Noise Reduction.....	12
1.3 Thesis Objectives	13
1.4 Thesis Structure.....	14
Chapter 2 Aeroacoustic and Aerodynamic Methods.....	16
2.1 Prediction of Serrated Trailing Edge Noise	16

2.2	Noise Model Derivation.....	19
2.2.1	Derivation of the General Case	21
2.3	Additional Modeling Methods	24
2.3.1	Overall Sound Pressure Level	24
2.3.2	Turbulent Boundary Layer Thickness Approximation.....	26
Chapter 3 Numerical Optimization.....		29
3.1	Definition of the Optimization Problems	29
3.2	Development of the Optimization Program	31
3.2.1	Algorithm Selection and Justification	31
3.2.2	General Structure of the Optimization Program.....	36
3.2.3	SA Algorithm	38
3.2.4	GRG Algorithm.....	40
3.3	Additional Numerical Methods.....	43
3.3.1	Calculation of the Objective Function.....	43
3.3.2	Calculation of the Numerical Derivatives	44
Chapter 4 Results and Discussion		47
4.1	Verification and Validation.....	50
4.1.1	Verification of SAGRSTEN.....	50
4.1.2	Verification and Validation of Noise Models.....	52
4.2	Single-Size Serrations	56
4.2.1	Sawtooth.....	56
4.2.2	Slitted.....	61
4.3	Frequency Dependent Serrations	66
4.3.1	Sawtooth.....	66
4.3.2	Slitted.....	70

Chapter 5 Conclusions.....	74
5.1 Summary and Contributions to the State of the Art	74
5.2 Conclusions	76
5.3 Future Work	78
5.3.1 Extensions on the Numerical Analysis and Optimization	79
5.3.2 Extensions into Experimental Studies	80
References	82

LIST OF TABLES

Table 4.1: Optimization trials and associated design variable bounds	48
Table 4.2: Optimized designs from each study and noise produced by each trailing edge	50

LIST OF FIGURES

Figure 1.1: Aircraft noise source contributions as a percentage of total noise produced during landing and take-off of a Boeing 777-300 (constructed using data from Ref. [13]).	3
Figure 1.2: Schematic of an airfoil, with a turbulent boundary layer incident on its surface, showing the production of TBL-TE noise through the interaction of turbulent structures with the trailing edge.....	5
Figure 1.3: Wing feather of the barn owl in different magnifications showing the structure of the trailing edge fringe (from Bachmann et al. [54]).....	12
Figure 2.1: 2-D schematic drawings of flat plate (a) straight, (b) sawtooth and, (c) slitted trailing edge extensions.....	20
Figure 3.1: Descriptive program flow chart for SAGRSTEN.	38
Figure 4.1: Design space plot of test optimization problem defined in Eqn. (4.1) with distribution of starting points (yellow and cyan triangles) and optimum points found (red triangles) shown.	51
Figure 4.2: SPL frequency spectrum (0.3 to 20 kHz) for straight and sawtooth trailing edges showing a comparison between Howe's model and experimental measurements (extracted from Ref. [45]).	54

Figure 4.3: SPL frequency spectrum (0.3 to 20 kHz) for straight and slitted trailing edges showing a comparison between Howe's model and experimental measurements (extracted from Ref. [45]).	54
Figure 4.4: SPL frequency spectrum (0.5 to 20 kHz) for straight and sawtooth trailing edges showing a comparison between Howe's model and large eddy simulation results (extracted from Ref. [92]).	55
Figure 4.5: Optimization study SS-Saw-2 SAGRSTEN convergence history of (a) the objective function in terms of the OASP, and (b) the sawtooth design variables h and λ .	58
Figure 4.6: SPL plotted as a function of frequency between 20 Hz and 20 kHz for optimum single size sawtooth trailing edge profiles.	59
Figure 4.7: Optimization study SS-Slit-1 SAGRSTEN convergence history of (a) the objective function in terms of the OASPL, (b) the slit design variable h , and (c) λ_1 and λ_2 .	63
Figure 4.8: SPL plotted as a function of frequency between 20 Hz and 20 kHz for optimum single size slitted trailing edge profiles.	64
Figure 4.9: SPL plotted as a function of frequency between 20 Hz and 20 kHz for optimum frequency-dependent sawtooth trailing edge profiles.	67
Figure 4.10: Optimum sawtooth amplitude plotted as a function of frequency between 20 Hz and 20 kHz for optimum frequency-dependent sawtooth trailing edge profiles.	67
Figure 4.11: Example of a Saw-Saw trailing edge serration profile design.	69
Figure 4.12: Example of a Saw+Saw trailing edge serration profile design.	69
Figure 4.13: SPL plotted as a function of frequency between 20 Hz and 20 kHz for optimum frequency-dependent slitted trailing edge profiles.	71

Figure 4.14: Optimum slit amplitude plotted as a function of frequency between 20 Hz and 20 kHz for optimum frequency-dependent slitted trailing edge profiles. 71

LIST OF ABBREVIATIONS

ANC	Active Noise Control
BFGS	Broyden–Fletcher–Goldfarb–Shanno
CAA	Computational Aeroacoustics
DV	Design Variable
GRG	Generalized Reduced Gradient
OASPL	Overall Sound Pressure Level
PNC	Passive Noise Control
SA	Simulated Annealing
SPL	Sound Pressure Level
SQP	Sequential Quadratic Programming
TBL	Turbulent Boundary Layer
TE	Trailing Edge

NOMENCLATURE

\mathbf{B}	Basis matrix
C_m	Friction velocity and mean shear interaction pressure constant
c	Chord length
E_n	Energy level at iteration n of the simulated annealing algorithm
∇F_R	Reduced gradient
f	Frequency
f_{\min}, f_{\max}	Lowest and highest frequencies in the frequency range of concern
f_{peak}^n	Frequency of the n^{th} SPL reduction peak
Δf_{peak}	Frequency bandwidth between adjacent SPL reduction peaks
f_{reduc}	Lowest frequency at which the serrated trailing edge produces less noise than the straight trailing edge
$G(\mathbf{x}, \mathbf{y}; \omega)$	Green's function

G_p	Green's function for the noise field from a point source without scattering
G_s	Green's function for the scattered noise field
g_i	i^{th} binding constraint
h	Serration amplitude (both sawtooth and slitted)
h_{\min}, h_{\max}	Smallest and largest feasible serration amplitudes
h_{opt}	Optimum serration amplitude
i	Imaginary number
$J(a)$	Example of an acoustic cost function from optimization literature
\mathbf{K}	Wavenumber vector
k_b	Boltzmann constant
m_{bc}	Number of currently binding constraints
m_{dv}	Total number of design variables
P_b	Turbulence blocked pressure
ρ	Probability of the simulated annealing algorithm accepting a point with greater energy
p_s	Scattered pressure
Re_c	Reynold's number based on chord length

T	Temperature of current simulated annealing iteration
T_0	Initial temperature for the simulated annealing algorithm
T_f	Final temperature for the simulated annealing algorithm
U	Mean flow speed
U_c	Convection velocity
u_*	Friction velocity
X_b	Vector of basic design variables
X_{nb}	Vector of non-basic design variables
x_1, x_2, x_3	Location of a far-field observer (Cartesian coordinate system)
x_1, x_2	Design variables in the optimization test case
y_1, y_2, y_3	Location of a point source in the vicinity of the trailing edge (Cartesian coordinate system)
Z	Objective function value
Z_{sc}	Scaled objective function value
$\tilde{Z}_{min}, \tilde{Z}_{max}$	Approximate minimum and maximum values of Z throughout the entire feasible design space

α	Angle between the x_3 axis and the far-field observer (in the x_1 - x_3 plane)
$\Gamma(x_3)$	Serration profile function
δ	Turbulent boundary layer thickness
δ_{DD}	Direc Delta function
ε	Integrated source layer thickness constant
ϵ	Machine epsilon
θ	Angle between the x_1 axis and the far-field observer (in the x_1 - x_2 plane)
\hat{i}_3	Unit vector parallel to the airfoil span
κ	Acoustic wavenumber
λ	Sawtooth serration width
$\lambda_{\min}, \lambda_{\max}$	Smallest and largest feasible sawtooth serration widths
λ_{opt}	Optimum sawtooth serration width
λ_1, λ_2	Slitted serration width and gap width
$(\lambda_1)_{\min}, (\lambda_1)_{\max}$	Smallest and largest feasible slitted serration slit widths
$(\lambda_2)_{\min}, (\lambda_2)_{\max}$	Smallest and largest feasible slitted serration gap widths
$(\lambda_1)_{\text{opt}}, (\lambda_2)_{\text{opt}}$	Optimum slitted serration slit width and gap width

λ_{1+2}	Total slitted serration width
$\lambda_{1/2}$	Serration slit-to-gap width ratio
ξ	Numerical derivative step size
ξ^*	Least error numerical derivative step size
$\varphi^*(\mathbf{y})$	Solution of the Laplace equation that describes irrotational flow around the serrated edge
ψ	Non-dimensional trailing edge noise spectrum
ψ_0	Straight edge non-dimensional trailing edge noise spectrum
ψ_{saw}	Sawtooth edge non-dimensional trailing edge noise spectrum
ψ_{slit}	Slitted edge non-dimensional trailing edge noise spectrum
Ω	Acoustic impedance
ω	Angular frequency

Chapter 1

INTRODUCTION

1.1 Motivation

Since the birth of aviation, in the early 1900's, aircraft noise has been an undesirable, yet seemingly unavoidable, side effect of flight. As the commercial aviation industry experienced growth, the number of people and communities exposed to aircraft noise also grew. What was initially an undesired side effect quickly became an unacceptable nuisance, which forced noise regulations onto the aerospace industry. As regulations tightened [1], noise reduction became a significant and important influence on the aircraft manufacturer's design process.

Throughout the 20th century, aircraft noise was considered a problem primarily because it is a nuisance [2]. At the turn of the century, researchers began investigating the effect that aircraft noise has on human health [3-6]. Studies regarding illnesses, annoyance, and learning disorders were conducted. The consensus from these studies was that regular and/or prolonged exposure to aircraft noise can have serious, negative effects on a human's health. The 2013 Hansell *et al.* British Medical Journal study stated specifically that there

is a “statistically significant association between exposure to aircraft noise and risk of hospitalization for cardiovascular diseases”.

The serious health issues caused by aircraft noise, along with numerous other social, economic and environmental issues, are a major issue for today’s aviation industry, and the problems are only becoming worse. There are currently over 3864 airports with scheduled commercial flights in operation across the world [7] that serviced over 33 million commercial flights in 2014 [8]. Within the next 20 years it is predicted that air traffic will at least double [9]. Further, the commercial aviation market is moving towards larger and faster aircraft, which will contribute to an increase in noise produced, per aircraft. As a direct result of increasing both flight volume and noise per aircraft, existing regulations concerning noise limits continue to become stricter [10], forcing aircraft into retirement. These factors establish a clear and definite motivation for aircraft noise minimization design. The most effective method of noise reduction is the direct elimination of noise at the sources; therefore, whenever possible, noise source reduction/elimination should be considered.

It is clear that aircraft noise is still a major, growing issue; however, over the years, improvements have been made in the design of low-noise systems and components. Since the mid-1900s, there has been a reduction of aircraft noise of approximately 20 EPNdB [11]. While this is an important step forward, nearly all of the reduction is attributed to improving the aeroacoustic performance of the engine, with less attention focused on airframe noise [12]. While the engines are a major source of noise during take-off, during approach and landing the engines are throttled down significantly. During these two phases of flight, the major source of noise is caused by the airflow interacting with the airframe.

An example of the proportionate take-off and landing noise is shown for a Boeing 777-300 in Figure 1.1.

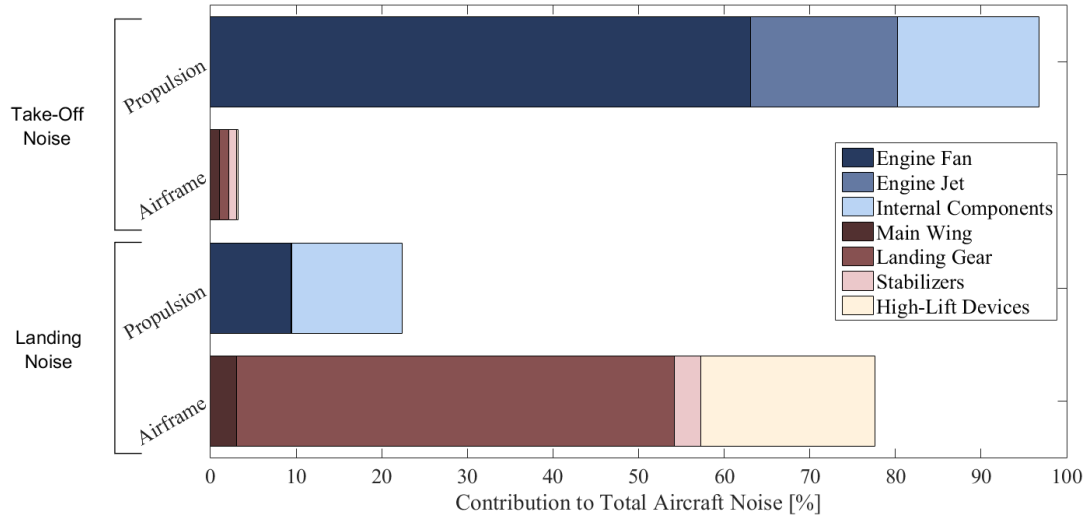


Figure 1.1: Aircraft noise source contributions as a percentage of total noise produced during landing and take-off of a Boeing 777-300 (constructed using data from Ref. [13]).

One of the main sources of airframe noise is produced by the trailing edge (TE) of surfaces that are exposed to the main stream of airflow [11, 14]. There has been a fair amount of research in this area; however, industry is reluctant to implement major TE noise reduction technologies. Reasons for the lack of adoption include the limitation in available design tools and too low of a cost-to-improvement ratio for current technologies. The work involved in this thesis aims to address both of these factors. Obtained results establish an advancement towards industry acceptance and application of trailing edge noise reduction technology.

1.2 Literature Review

In this section, an overview of the relevant research in TE noise is presented. The focus of this review is on the mechanisms responsible for the production of TE noise, methods of TE noise prediction, as well as methods of TE noise reduction. In particular, research on TE serrations as a means of noise reduction is reviewed.

1.2.1 Production of Trailing Edge Noise

The noise created by turbulent events, occurring in an airfoil's boundary layer, interacting with the airfoil's own solid surfaces, is known as airfoil self-noise. During the 1980s, in an effort to understand and predict the mechanisms of airfoil self-noise, a series of research studies was conducted at, and supported by, the NASA Langley Research Center [15]. From the research effort, Brooks *et al* [15] identified five mechanisms that are responsible for the airfoil self-noise, which are the following:

- (i) Turbulent boundary layer – trailing edge (TBL-TE) noise
- (ii) Laminar boundary layer – vortex shedding noise
- (iii) Separation-stall noise
- (iv) Trailing edge bluntness – vortex shedding noise
- (v) Tip vortex formation noise.

Airfoil self-noise can range from being highly tonal to fully broadband. The nature of the self-noise spectrum is dependent on which of the above five mechanisms is dominant. Broadband airfoil self-noise is attributed to mechanism (i), while tonal airfoil self-noise arises from any of mechanisms (ii) - (v). The work presented in this thesis pertains exclusively to the broadband airfoil self-noise, and thus it focuses on mechanism (i).

In many cases, the most prevalent noise source of the mechanisms listed above is TBL-TE noise [16, 17]. Turbulent boundary layer – trailing edge noise is produced by coherent structures, or eddies [18], in a TBL interacting with the trailing edge of a solid surface, as they convect downstream. Noise is produced from this interaction because of the sudden change in the flow domain, i.e., the wall boundary condition, enforced by the solid and rigid surface, instantaneously vanishes at the TE. This domain change can be viewed as a sudden discontinuity in the acoustic impedance, which causes the surface pressure (created from eddies that are incident on the solid surface) to scatter into acoustic waves, thus producing sound [19]. The TBL-TE noise production mechanism can occur for any surface that has a trailing edge, and is exposed to flow conditions producing an incident TBL. As an example, and to give some graphical context to the problem, the TBL-TE noise mechanism is depicted in Figure 1.2 for an airfoil.

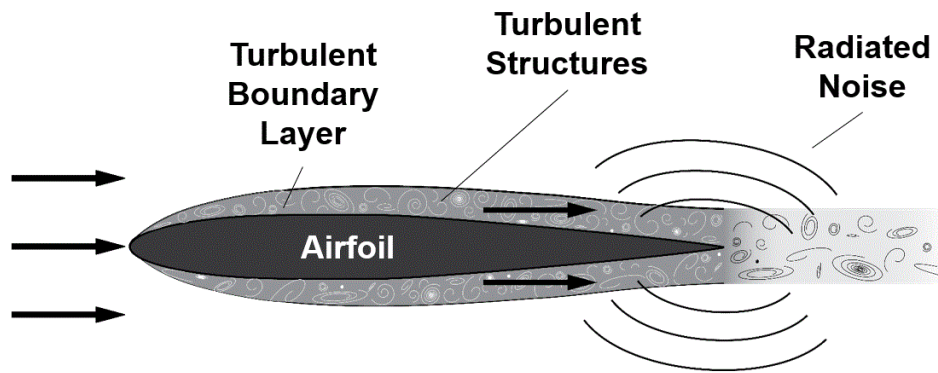


Figure 1.2: Schematic of an airfoil, with a turbulent boundary layer incident on its surface, showing the production of TBL-TE noise through the interaction of turbulent structures with the trailing edge.

There has been a significant amount of research conducted regarding TBL-TE noise including experimental testing [15, 20-25], numerical simulations [26-30], and analytical-based noise modelling [31-40]. This thesis investigates analytical-based TE noise prediction methods; therefore, this review does not cover details regarding numerical and

experimental studies. The first examination of low Mach number, TE noise was carried out by Powell in 1959 [41]. Powell's analysis used similarity arguments to estimate the strength of dipole sources that were assumed to exist on the surface, near the TE. Additional TE noise modeling methods and theories, however, did not emerge until over a decade later. The contributions to TE noise research during this time were numerous (see Ref. [38] for a detailed review), and notable developments were made by Ffowcs Williams and Hall [31], Chase [34], and Amiet [36]. The first of these additional noise models was derived by Ffowcs Williams and Hall [31] using Lighthill's acoustic analogy. Their model gives the radiated noise from a turbulent flow convecting past a semi-infinite, rigid plate with a zero thickness and at a zero angle of attack. The Ffowcs Williams and Hall model was able to predict the shape of the radiation field, and the effects of flight relative to an observer's position, which were both improvements over Powell's model. Several years following the publication of Ref. [31], Chase [32] produced his own model using diffraction theory instead of Lighthill's acoustic analogy. Similar to the Ffowcs Williams and Hall model [31], Chase's model could predict the radiated field shape and flight effects; however, it had the added benefit of not having to explicitly consider the Lighthill sources. Instead, Chase [32] quantified the sources using a turbulent pressure spectrum model, which is based on experimental data.

The majority of research regarding the development and analysis of mathematical models for the prediction of TBL-TE noise can be fit into one of two derivation methods. The most significant contributions to original work on the two methods were published in the 1970s, by two researchers, Amiet [35-37], and Howe [38], respectively. The basis on which Howe's model is developed was first established by Chase [32, 34] and

Chandiramani [33]. The concepts proposed in those publications were then solidified into one TBL-TE noise model by Howe [38]. The initial work on Amiet's model [35-37] was conducted by him shortly after publication of Chase and Chandiramani's work. Several decades later, Roger and Moreau [39, 40] extended Amiet's model to account for back-scattering effects.

Both the Amiet and Howe models predict the broadband far field noise spectrum radiated as a result of TBL structures convecting over the TE of a rigid surface. The two models are very similar; however, the main difference arises in the method by which the near field pressure fluctuations are related to acoustic radiation propagating into the far field. In Ref. [36], Amiet states the following two specific differences that contribute to this. First, the basis of Howe's model uses Green's function for zero mean flow, while Amiet's model considers the effects of a non-zero mean flow velocity, U . Second, Amiet assumes equal, anti-correlated, acoustic radiation into the regions above and below the plane of the flat plate, whereas the Howe model assumes radiated fields above and below the plane that are not equal (as a result of turbulent flow on one side of the flat plate).

1.2.2 Trailing Edge Serrations

Over the past several decades, a number of different methods have been studied for reducing TBL-TE noise. In all methods, the objective is to reduce or soften the acoustic impedance discontinuity between the solid surface of the airfoil and free space. The specific mechanism through which this softening occurs is different for each method; however, they can be generally classified as either active noise control (ANC) methods or passive noise control (PNC) methods. ANC is defined as a method of reducing noise using a control system to produce a noise-canceling response signal [42]. In general, ANC

systems employ a sense-analyze-respond format where an undesirable event is sensed, a response is generated, and then initiated to reduce or cancel noise. Active methods investigated include TE blowing/suction, responsive control of TE cross-sectional profile. Passive noise control methods reduce noise through a fixed-state interaction with the fluid domain in which the noise is produced and/or propagating. Noise reduction methods that are passive in nature include TE serrations, TE brush extensions, aeroacoustically designed airfoil profiles, increased material porosity near the TE, flexible TE, and various combinations of these.

Each of the methods listed above have shown different levels of success in TBL-TE noise reduction. ANC methods tend to perform well to reduce low frequency, tonal noise, while the opposite is true for PNC methods. In addition to aeroacoustic performance; however, other considerations, relevant to the aviation industry, should be evaluated when comparing methods. Additional considerations include, for example, cost of maintenance, and added weight. Considering other, non-acoustic, factors will help to ensure the development of designs that have a high chance of industry acceptance. From this perspective, passive methods are, in general, more beneficial than active ones for typical aerospace applications. Two main issues with ANC are:

- (i) Greater number of components, and
- (ii) Power is required to operate the control system.

In general, as the number of components required increases, both the cost of maintenance and the net system weight will also increase. An ANC system requires power for the sensors, controller electronics, and, most significantly, the response actuators. The net result of (i) and (ii) is a greater cost of operation, which ultimately is a major deterrent to

industry acceptance. It should be noted, however, that in the current age of rapid expansion and development of digital technology (leading to simpler, smaller, and lower-power electronics), both of these arguments are becoming less significant.

After considering the aeroacoustic performance observed experimentally, and the outstanding performance predicted from theory in addition to secondary factors mentioned above, one of the most promising methods is the use of TE serrations. Using serrations for airfoil noise reduction was originally studied as an airfoil leading edge modification. In 1980, Fink and Bailey [43] published acoustic wind tunnel results of several different airframe reduction concepts; trailing edge serrations being one of them. More than a decade later, M. S. Howe [44, 45] published his semi-empirical model for predicting the TBL-TE noise produced by a serrated TE. Howe's model is an extension of his own model for TBL-TE noise produced by an unmodified, straight TE [38], and is formulated such that a derivation of the model for any serration geometry can be obtained. A more detailed explanation of the derivation of Howe's model is given in Chapter 2. Howe first published the model for a sinusoidal serration geometry [44], and shortly after, for a sawtooth serration geometry [45]. In recent years, Howe's model has been re-derived by other researchers for additional geometries including slits [46] and various, superimposed, combinations of the sinusoidal, sawtooth and slit serrations [47].

Up until very recently, Howe's model was the only method for predicting serrated TBL-TE noise without obtaining experimental results or conducting numerical simulation studies, which are both very costly and time consuming. In 2016, Lyu *et al.* [48] developed another model for serrated TBL-TE noise prediction (referred to in this thesis as Lyu's model), which is based on Amiet's [35-37] un-modified TE model. Lyu *et al.* state that the

new model is more consistent with experimental results, and that it yields more realistic predictions than Howe's model. No direct comparison was given between Lyu's model and experimental results, and since the publication of Ref. [48], there has been no additional study of the model. Therefore, for these reasons, and based on the timeframe of this thesis, the focus is given to Howe's model, and consideration of Lyu's model in this work is limited to Section 5.3 - Future Work.

1.2.3 Influence of Nature on Serration Design

Evolution, the time-dependent development process seen in nature, is arguably the most ideal form of design optimization known, and examples of its effectiveness are seen everywhere. In the case of airfoil self-noise reduction, the prime example is the owl's wing. The owl is incredibly effective at reducing noise from its wings, and is dependent on its advanced acoustical abilities for survival [49]. Further, it is the only known flying vehicle (fabricated or natural) capable of near silent flight [50]; therefore, much can be learned from studying the flight of owls and their anatomy. Long before research started on TBL-TE noise reduction, work was being done to investigate how owls, unlike other birds, are able to fly so quietly. R.R. Graham [51] was the first to identify three specific attributes, which are directly related with the owl's impressive aeroacoustic performance. Originally published in 1934, Graham's three attributes are:

- (i) Comb-like structure of the feathers on the wing's leading edge;
- (ii) Fringed feather edges at the wing's trailing edge;
- (iii) Velvety upper surface of the wing and a downy lower surface.

At the time of discovery, Graham could not explain exactly how, or in what proportion, these three attributes contributed to the owl's silent flight; only, that these were unique

differences to the wings of almost all other birds. Many years later, Graham's attributes were proven experimentally by Kroeger *et al.* [52] in their 1971 study. The study involved measuring the owl's flight noise both before and after modification/removal of each of attributes (i)-(iii).

By comparing Graham's attributes to the literature on TBL-TE noise reduction methods, it is apparent that the two are closely linked. Whether or not researchers have been directly inspired by these attributes, they are highly relevant in all work regarding TBL-TE noise minimization. Of specific importance to the work in this thesis is attribute (ii), the trailing edge fringes, which are shown in Figure 1.3. The TE fringes create a smooth transition from the wing surface to the freestream, thereby interfering with the acoustic scattering process at the TE, typically observed [53]. Specifically, flat plate serrated trailing edge extensions simulate the geometry of the fringe at the TE of an owl's wing. This 2D representation is not an exact replication of an owl's TE fringe as it does not account for certain features such as elasticity. Bachmann and Wagner [53] state that the fringes are so pliant that they are free-floating in the flow. The effect that this feature has on the noise reduction performance has not been commented on in the literature, and no noise prediction methods currently exist that account for non-stiff TE serrations. Additionally, in a study of noise reduction using TE brush extensions, Herr [54] found that, while brush fiber flexibility is generally beneficial, it is not a prerequisite to obtain noise reduction.

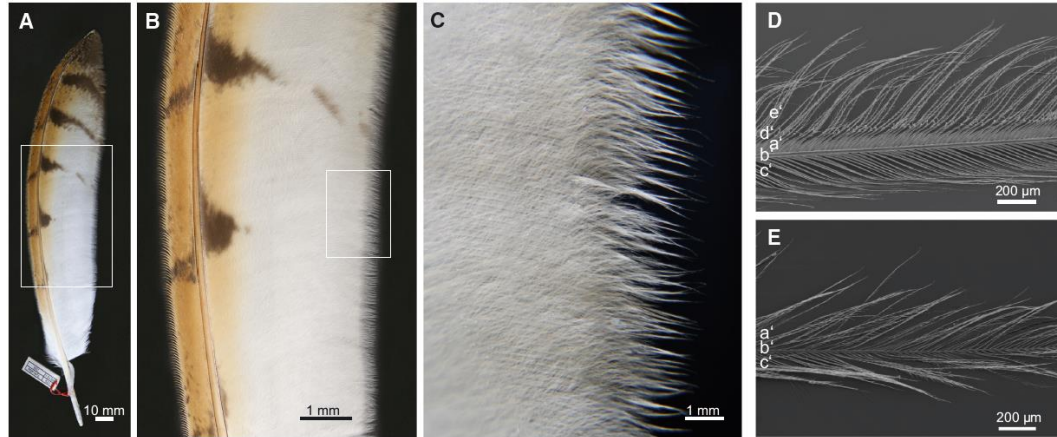


Figure 1.3: Wing feather of the barn owl in different magnifications showing the structure of the trailing edge fringe (from Bachmann et al. [55]).

1.2.4 Optimization for Trailing Edge Noise Reduction

To date, little work has been done in optimization of the serrated trailing-edge shape for noise reduction. There has been, however, some attention directed towards optimizing the cross-sectional shape of an airfoil to minimize trailing edge noise, and in some cases, to improve the aerodynamic performance. Some of the initial work in searching for an acoustically optimized airfoil was conducted as part of the European-based wind turbine project, DATA [56]. This project did not employ computational optimization methods, but instead took the approach of identifying the sensitivity of TBL-TE noise to key flow parameters. Using the sensitivity information, several airfoil designs were then manufactured and tested. The test results revealed that the new designs produced less TBL-TE noise than the original airfoils; therefore, confirming that TE optimization can produce improved designs [57].

Early studies that used computational optimization methods to reduce airfoil self-noise only incorporated noise as an additional/secondary consideration for defining an objective function that describes an airfoil's overall performance [58]. In the early 2000s, several important studies, which emphasized optimizing airfoils for noise reduction, were

published by Marsden *et al* [59-62] and Lutz *et al* [63]. The work of both sets of authors was based on defining the flow domain around the trailing edge by numerically solving the Navier-Stokes equations. Marsden used the large eddy simulation method, while Lutz *et al.* chose the Reynolds averaged Navier-Stokes method. The properties of the flow field near the trailing edge were then used in acoustic models to quantify the noise produced by the trailing edge, for use in the objective function. For the optimization method, Marsden *et al.* used a gradient-based algorithm, called the method of “incomplete sensitivities”, which is similar to a steepest descent method except that the large eddy simulation is solved only once per derivative calculation. Calculation of the derivative is done by approximating the perturbed objective function values to be used in the finite difference equation. Instead of a gradient-based algorithm, Lutz *et al.* used a derivative-free, genetic algorithm for the optimization.

1.3 Thesis Objectives

The overall aim of this thesis is to advance the state of noise reduction from TE modification research and development towards industry acceptance and implementation. To achieve this goal, the following objectives are addressed in this thesis:

- (i) To develop a framework for the aeroacoustic optimization of trailing edge modifications, as a tool for designing minimum-noise structures
- (ii) To investigate theoretical optimum geometries of flat-plate, serrated trailing edge extensions, and identify conditions of optimality through a series of optimization studies.

1.4 Thesis Structure

This thesis describes the methods and results of optimization studies, in which the TBL-TE noise, produced by flat-plate serrated TE extensions, is minimized through the modification of the serration geometry. Context is established for the topic of TE noise reduction, analysis methods are described, analysis results are presented, and concluding remarks are provided. A more specific description of each chapter's contents is given in the remaining paragraphs of this section.

The current chapter (Chapter 1) defines the problem being addressed, and provides the motivation for this work. A summary of relevant literature, which has contributed to the state of the art, is also presented. The literature review is given to provide context for the work, and to create a clear indication of the void in research that is being addressed by this thesis.

Chapter 2 and Chapter 3 describe the methodology used in the setup and execution of the optimization studies. Chapter 2 describes the methods used to model the aeroacoustic noise produced by the trailing edge, as well as other, associated, aerodynamic models. Chapter 3 presents the details of the optimization algorithm and numerical methods, used to develop the in-house optimization program. Also included in Chapter 3 are a description of the optimization program, SARGSTEN, and a summary of its main functions. SARGSTEN was written in-house by the author specifically for the optimization of TE modifications.

Chapter 4 presents the results of the optimization studies and associated analyses. A discussion of the results is then given. The results presented in Chapter 4 are divided into four sections according to the type of optimization study they belong to, i.e., serration

geometry and optimization frequencies. The sections are given sequentially as broadband, sawtooth serration results; broadband, slitted serration results; narrowband, sawtooth serration results; and narrowband, slitted serration results.

Chapter 5 presents conclusions obtained from completion of this work, as well as the potential directions in which future work may continue.

Chapter 2

AEROACOUSTIC AND AERODYNAMIC METHODS

The methods used to evaluate the aeroacoustic and aerodynamic properties are presented in this chapter. The theoretical basis and key assumptions required for the serrated TBL-TE noise model used in this thesis are presented and discussed first, accompanied by the justification for selecting it over other methods of TBL-TE noise prediction. Detailed steps of the derivation of the noise model then follow in the next section with comments on where assumptions and simplifications/idealizations enter the model. At the end of the chapter, several other important aerodynamic and acoustic models/equations used in this study are presented along with a thorough justification for their use.

2.1 Prediction of Serrated Trailing Edge Noise

Aircraft noise, and associated design challenges, cannot be isolated from other competing factors that influence the design and production of aircraft in today's aviation

industry. For example, a complete and thorough optimization study of a certain aircraft design must consider and weigh the effects of fuel efficiency, passenger comfort, safety rating, frequency of maintenance, etc., in addition to noise production. Fast and efficient numerical methods are therefore desirable for the evaluation of TBL-TE noise, used as the objective function value in an optimization study [11].

One possible method is the use of numerical simulations that predict the generation of aeroacoustic noise, known as computational aeroacoustics (CAA). The use of CAA programs is growing in popularity due to the sustained exponential growth of available computational power from year to year. While it is becoming possible, and slightly more practical, to use such programs for noise prediction, they remain to be time consuming, inefficient and costly. This is specifically true when comparing relative to other segments of an aircraft's design optimization. Similarly, experimental aeroacoustic studies are also, slow, inefficient and costly, but to a much greater extent.

It is clear that neither CAA nor experiments satisfy the maximum efficiency, minimum run-time, and reasonable cost requirements for implementing aircraft noise reduction into the complete design optimization framework. Semi-empirical models for prediction of the TBL-TE noise then present themselves as a viable alternative. The main reason for this is that the noise can be calculated almost instantaneously, and with very little computational power, therefore satisfying all three requirements. The models are, however, still in continuous development and research efforts are currently focused on understanding the noise generating/reduction mechanisms. The main weakness in using these models, therefore, is that their level of accuracy is lower compared to CAA and experimental data. While the accuracy cannot be ignored, it in itself does not outweigh the other major benefits

of using semi-empirical models instead of CAA or experiments. Further, a significant amount of attention is now being directed towards research on the use and development of semi-empirical TE noise models, the most recent work being done by Lyu *et al.* [48]. As research in this field continues to grow and develop, current and new noise models will rapidly become more accurate, thus making them even more applicable for use in the aircraft design optimization procedure. It is for this reason, combined with their inherent computational efficiency, that the use of a semi-empirical noise model is thoroughly justified for the optimization work in this thesis.

The theoretical basis and overall approach for Howe's serrated TBL-TE noise model was initially proposed two decades before the release of Howe's publications in the work of both Chandiramani [33] and Chase [34], which was later combined into one theory in Ref. [38]. The TBL-TE noise is mathematically modeled as an evanescent pressure wave, incident on the rigid, planar surface, being scattered into far-field acoustic pressure radiation by the TE. The trailing edge scatters the near-field pressure wave as a result of the sudden discontinuity in the acoustic impedance, Ω , in the direction perpendicular to the plane of the rigid surface. Ω is directly proportional to the density of the medium through which the wave is travelling. The planar surface is rigid, and therefore its density is effectively infinite, whereas the density of air is on the order of 1 (in S.I. units). This abrupt change in density is what creates the discontinuity, which scatters the wall pressure into radiated sound.

2.2 Noise Model Derivation

The theory and assumptions used to develop Howe's semi-empirical model [44, 45] for the TBL-TE noise produced by a flat plate TE extension are presented in this section.

Throughout the derivation, the following assumptions are made:

- (i) Turbulence measured slightly upstream of the edge is frozen in its measured state while it convects downstream and interacts with the edge;
- (ii) The physical model, shown in Figure 2.1, is of infinite span;
- (iii) The Kutta condition is satisfied at the trailing edge (i.e., velocity and pressure are finite at the TE [19]);
- (iv) The main flow (outside of the boundary layer) is of low Mach number and is two-dimensional;
- (v) Noise produced by the TBL interacting with the TE is the only source of noise present;
- (vi) Scattered field has no effect on the incident field, i.e., no back reaction.

Detailed schematics of the three geometries considered in this thesis are given in Figure 2.1, which are the basis for the development of Howe's model. The mathematical equations that define the spanwise-periodic TE geometry shown in Figure 2.1 (b) and (c) are also given below in Eqns. (2.1) and (2.2), respectively.

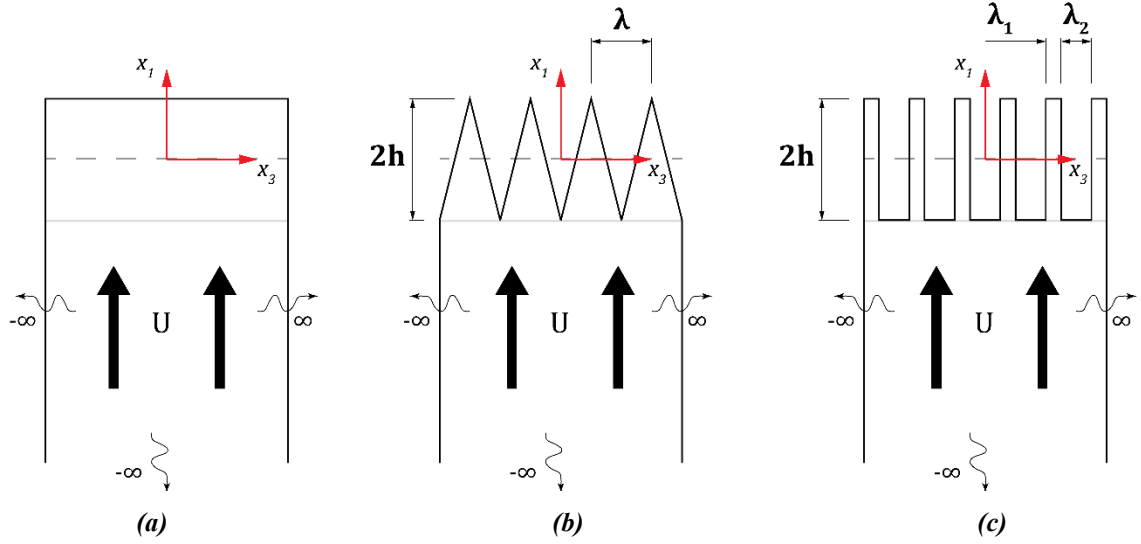


Figure 2.1: 2-D schematic drawings of flat plate (a) straight, (b) sawtooth and, (c) slitted trailing edge extensions

$$x_1 = \Gamma(x_3) = \begin{cases} \left(\frac{4h}{\lambda}\right)(x_3 - n\lambda), & n\lambda < x_3 < \left(n + \frac{1}{2}\right)\lambda, \\ \left(\frac{-4h}{\lambda}\right)(x_3 - n\lambda), & \left(n - \frac{1}{2}\right)\lambda < x_3 < n\lambda, \end{cases} \quad (2.1)$$

$$n = 0, \pm 1, \pm 2, \dots$$

$$x_1 = \Gamma(x_3) = \begin{cases} h, & (n + 1)\lambda_1 + n\lambda_2 < x_3 < (n + 1)(\lambda_1 + \lambda_2), \\ -h, & n(\lambda_1 + \lambda_2) < x_3 < (n + 1)\lambda_1 + n\lambda_2, \end{cases} \quad (2.2)$$

$$n = 0, \pm 1, \pm 2, \dots$$

where h is the serration amplitude (with $2h$ being the root-to-tip distance) measured in the streamwise direction, λ is the sawtooth serration width, λ_1 is the slitted serration tooth width, and λ_2 is the slitted serration gap width.

Equations (2.1) and (2.2) define the serrated trailing edge geometry in terms of the positive streamwise extent of the rigid, flat plate, x_1 , as a function of the geometrical variations in the spanwise direction, x_3 . Since TBL-TE noise is produced, and consequently radiated into the far-field, when turbulent structures in the boundary layer interact with the

edge discontinuity, the magnitude and location of this production is highly dependent on the location of the local edge. It can therefore be seen that Eqns. (2.1) and (2.2) quickly become a crucial part of calculating the noise for their respective TE geometries.

2.2.1 Derivation of the General Case

The scattered pressure, p_s , produced at the trailing edge is defined in terms of a greens function and the turbulence blocked pressure, P_b as follows:

$$p_s(\mathbf{x}, \omega) = \frac{i}{2} \int_{-\infty}^{\infty} dy_3 \int_{-\infty}^0 dz_1 \int_{-\infty}^{\infty} \gamma(\mathbf{K}) \times [G(\mathbf{x}, y_1, y_3; \omega)] P_b(\mathbf{K}, \omega) e^{i[K_1 y_1 + K_3 y_3]} d^2 \mathbf{K} \quad (2.3)$$

where, \mathbf{x} is the vector of Cartesian components for the location of the far-field observer, \mathbf{y} is the vector of Cartesian components for the location of a point source in the vicinity of the TE, $z_1 = y_1 - \Gamma(y_3)$, and the wavenumber function, $\gamma(\mathbf{K})$, is calculated from the acoustic wave number, κ , as:

$$\gamma(\mathbf{K}) = \begin{cases} \sqrt{(\kappa^2 - \mathbf{K}^2)}, & \text{for } \mathbf{K} < \kappa \\ i\sqrt{(\mathbf{K}^2 - \kappa^2)}, & \text{for } \mathbf{K} > \kappa \end{cases} \quad (2.4)$$

The Green's function in Eqn. (2.3) is the solution of the inhomogeneous, reduced wave equation, Eqn. (2.5), and defines an acoustic point source located near a sharp edge as a function of its position relative to the edge, \mathbf{y} .

$$(\nabla^2 + \kappa^2)G(\mathbf{x}, \mathbf{y}; \omega) = \delta_{DD}(\mathbf{x} - \mathbf{y}) \quad (2.5)$$

where δ_{DD} is the Dirac delta function, and ∇^2 is the Laplacian. The following two conditions must be satisfied for $G(\mathbf{x}, \mathbf{y}; \omega)$ to be a suitable Green's function for this problem:

(i) $G(\mathbf{x}, \mathbf{y}; \omega)$ must have a vanishing normal derivative on the plate's rigid surface everywhere upstream of the TE, i.e., $\partial G / \partial x_2|_{x_2=0} = 0$ for $x_1 < \Gamma(y_3)$;

(ii) The Kutta condition is satisfied at the TE.

An expression for this Green's function is obtained by solving the classical Sommerfeld diffraction problem [64]. Crighton and Leppington [65] show that a solution to this problem can be obtained by setting $G(\mathbf{x}, y_1, y_3; \omega)$ equal to the following summation:

$$G(\mathbf{x}, y_1, y_3; \omega) = G_p(\mathbf{x}, y_1, y_3; \omega) + G_s(\mathbf{x}, y_1, y_3; \omega) \quad (2.6)$$

where G_p represents the field from a point source without scattering, and G_s represents the scattered field. For a semi-infinite rigid surface, the terms on the right hand side of Eqn. (2.6) are given in Ref. [64, 66], by the following expressions:

$$G_p(\mathbf{x}, \mathbf{y}; \omega) = \frac{-e^{ik|\mathbf{x}-y_3\hat{\mathbf{t}}_3|}}{4\pi|\mathbf{x}-y_3\hat{\mathbf{t}}_3|}, \quad (2.7)$$

$$G_s(\mathbf{x}, \mathbf{y}; \omega) = \frac{-\sqrt{k} \sin^{1/2}(\alpha) \sin(\theta/2) \varphi^*(\mathbf{y}) e^{ik|\mathbf{x}-y_3\hat{\mathbf{t}}_3|}}{\pi\sqrt{2\pi i}|\mathbf{x}-y_3\hat{\mathbf{t}}_3|} \quad (2.8)$$

where α is the angle in the x_1 - x_3 plane between the x_3 axis and the far-field observer, θ is the angle in the x_1 - x_2 plane between the x_1 axis and the far-field observer, $\hat{\mathbf{t}}_3$ is the unit vector parallel to the airfoil span, and $\varphi^*(\mathbf{y})$ is a solution of the Laplace equation that describes irrotational flow around the serrated edge [45].

The turbulence blocked pressure, P_b , in Eqn. (2.3) represents the pressure fluctuations on a plane, rigid wall produced by turbulent structures in a TBL convecting over the surface. Due to the random and chaotic nature of a TBL, no purely analytical model of reasonable accuracy exists to predict the value of P_b . There are, however, a number of models that yield accurate predictions of the turbulent wall pressure wave-number-

frequency spectrum, which are developed from experimental data. The model used for P_b was developed through dimensional analysis by Chase [67] and is expressed as:

$$P_b(\mathbf{K}, \omega) = \frac{C_m \rho^2 u_*^3 K_1^2 \delta^5}{\left[\left(K_1 - \omega/U_c \right)^2 \left(\delta U_c / 3u_* \right)^2 + (\mathbf{K}\delta)^2 + \varepsilon^2 \right]^{5/2}} \quad (2.9)$$

where δ is the TBL thickness, the friction velocity, $u_* \approx 0.0352U$, the convection velocity, $U_c \approx 0.7U$, and the empirical constants, $C_m = 0.1553$, and $\varepsilon = 1.33$. The value of C_m corresponds to the P_b contribution from the interaction of the friction velocity with the mean shear [19], and the reciprocal value of ε corresponds to the integrated source layer thickness as a fraction of δ [67]. This wall pressure spectrum model was chosen because, according to Chase [67], Eqn. (2.9) yields a good approximation for $P_b(\mathbf{K}, \omega)$, specifically in the convective domain. For flow structures, defined by U/ω , smaller than δ (i.e., $\omega\delta/U > 1$), and at low Mach numbers, the largest magnitude of wall pressure fluctuations occur within the convective ridge of the wavenumber-frequency spectrum [19]. The convective ridge occurs where the streamwise wavenumber, K_1 , is within $|\omega/U_c - \omega/U|$ of ω/U_c which, in a physical sense, defines the size of flow structures that convect downstream within the TBL. Since the wall pressure is dominated by streamwise wavenumbers within this region, an unbounded integration with respect to K_1 can be approximated by evaluating the integrand at $K_1 = \omega/U_c$ and $\kappa = 0$ (since $\kappa \ll |K|$ for low Mach numbers). These approximations are necessary in order to obtain numerical estimates for the serrated TBL-TE noise, and have a reasonably small effect on the values obtained [44].

The final forms of the non-dimensional edge noise spectrum for the straight, sawtooth and slitted trailing edge geometries are given below in Eq. (2.10) to (2.12), respectively.

$$\psi_0(\omega) = \frac{\left(\frac{\omega\delta}{U_c}\right)^2}{\left[\left(\frac{\omega\delta}{U_c}\right)^2 + \varepsilon^2\right]^2} \quad (2.10)$$

$$\psi_{\text{saw}}(\omega) = 8 \left(\frac{h}{\delta}\right)^2 \left(\frac{\omega h}{U_c}\right)^2 \times \sum_{n=-\infty}^{\infty} \frac{\left[1 - \frac{\cos\left(\frac{2\omega h}{U_c}\right)}{\cos(n\pi)}\right] \left[\left(\frac{\omega h}{U_c}\right)^2 + \left(2n\pi \frac{h}{\lambda}\right)^2\right]}{\left[(n\pi)^2 - \left(\frac{2\omega h}{U_c}\right)^2\right]^2 \left[\left(\frac{\omega h}{U_c}\right)^2 + \left(2n\pi \frac{h}{\lambda}\right)^2 + \left(\frac{\varepsilon h}{\delta}\right)^2\right]^2} \quad (2.11)$$

$$\psi_{\text{slit}}(\omega) = \sum_{n=-\infty}^{\infty} \Theta \Theta^* \frac{\left[\left(\frac{\omega\delta}{U_c}\right)^2 + \left(2n\pi \frac{\delta}{(\lambda_1 + \lambda_2)}\right)^2\right]}{\left[\left(\frac{\omega\delta}{U_c}\right)^2 + \left(2n\pi \frac{\delta}{(\lambda_1 + \lambda_2)}\right)^2 + \varepsilon^2\right]^2} \quad (2.12)$$

$$\Theta(K, \lambda_1, \lambda_2, h) = n^{-1} \left[\left(e^{\frac{2in\pi\lambda_1}{(\lambda_1 + \lambda_2)}} - 1 \right) e^{iK_1 h} + \left(1 - e^{\frac{-2in\pi\lambda_2}{(\lambda_1 + \lambda_2)}} \right) e^{-iK_1 h} \right] \quad (2.13)$$

Equations (2.11) and (2.12) are obtained by substituting (2.1) and (2.2) into Eqn. (2.3), respectively. For the straight, un-modified edge, Eqn. (2.10) can be obtained by setting the value of h to zero in a manipulated version of Eqn. (2.11) (i.e., a sawtooth of zero height is a straight line).

2.3 Additional Modeling Methods

2.3.1 Overall Sound Pressure Level

The overall sound pressure level (OASPL) is used frequently in this thesis as the representative value for the amount of noise created by the TBL-TE aeroacoustic mechanism. The general definition of the OASPL is given in Eq. (2.14) and it should be noted that the dB reference value used here is one (not the typical value of 2.0×10^{-5} Pa). The change in reference is due to the use of the non-dimensional noise parameter, ψ , in place of an ensemble-averaged, squared, acoustic pressure. Due to these adjustments from the typical definition of OASPL, the values obtained using Eq. (2.14) have no physical meaning on their own, and must only be used for direct comparisons. This limitation is not an issue in the studies presented in this thesis, as all results obtained are compared to those from either a straight, un-modified edge and/or another modified TE design.

$$\text{OASPL} = 10 \text{Log}_{10} \left[\int_{\omega_{\min}}^{\omega_{\max}} \psi(\omega) d\omega \right] \quad (2.14)$$

The OASPL does not possess any information about the distribution of the pressure signal across the frequency spectrum; however, it does provide an effective means of representing the noise in a single value. Representing the noise in this way is essential to the optimization procedure, which requires a single value for the objective function to evaluate each combination of the attempted design variables. Similar methods of using the OASPL to obtain a single value for the objective function were successfully implemented by both Jones *et al.* [68], and Marsden *et al.* [62]. In the Jones *et al.* TE noise optimization study, the OASPL was calculated in a similar manner to Eqn. (2.14) except that, instead of a continuous integration across all relevant frequencies, a discrete summation of $\text{SPL}_{1/3}$ at

each 1/3 octave band was used. Marsden *et al.* did not specifically use the OASPL in their study, but their derivation of an acoustic cost function, $J(a)$, is essentially the same. In Ref. [62], $J(a)$ is simply equal to the integration of the acoustic pressure frequency spectrum (across all desired frequencies); therefore, the only difference between it and Eqn. (2.14) is that the OASPL integral is converted to a magnitude.

An alternative method to calculating the OASPL (for obtaining a single, representative value of the pressure signal) is to use the single maximum value of the sound pressure level (SPL) frequency spectrum. The benefit of this method is that it is more computationally efficient because a basic 1-D maximum value search is performed in place of the numerical integration required in Eqn. (2.14). Bertagnolio *et al.* [69] states that similar optimization results are obtained when either the max value, SPL_{max} , or the OASPL are used as the objective function; however, this may not always be the case. A major issue with using the SPL_{max} value for the objective function is its sensitivity to narrowband, or tonal, spikes in the SPL spectrum. For example, a design may have an SPL frequency spectrum with a large spike in SPL at a particular frequency, but relatively moderate values of SPL at all other frequencies in the range of concern. In such a case, SPL_{max} does not sufficiently characterize the full noise spectrum of that design and may produce optimization results that only reduce noise in a narrow band of frequencies near SPL_{max} .

2.3.2 Turbulent Boundary Layer Thickness Approximation

The TBL thickness used in the noise prediction models defined in Eqns. (2.10) - (2.12) was calculated using the following equation:

$$\delta = \frac{0.37c}{\text{Re}_c^{1/5}} \quad (2.15)$$

where c is the chord length (the streamwise distance between the leading and trailing edges in the case of a flat plate), and Re_c is Reynolds number based on the chord length.

Equation (2.15) is Prandtl's power-law model for a turbulent boundary layer over a flat-plate [70]. This method is both a simplification and idealization for predicting the TBL thickness; however, its use is justified for the context of the current study. An alternative method for calculation of the TBL thickness is to use the publicly available airfoil analysis software package XFOIL (or other similar software package). Using the panel method, XFOIL calculates the pressure distribution across an airfoil's surface for a user-defined 2D airfoil geometry, Reynolds number and Mach number, which is then used to calculate other aerodynamic properties [71]. Several publications related to the work in this thesis have used XFOIL to calculate the TBL thickness [63, 68, 69, 72]; however, in these studies only the 2D airfoil profile is modified. Therefore, the TBL thickness, calculated by XFOIL, is constant in the direction perpendicular to the airfoil cross-section. XFOIL has also been used to calculate the TBL thickness, and other parameters, in serrated TE noise studies [73]; however, poor accuracy resulted from its use in such a situation. Gruber [73] reported that the variation in critical Strouhal number (which he used to mark the occurrence of a specific event in the serrated TE noise frequency spectrum) was observed to be $\pm 30\%$ and attributed this, almost entirely, to XFOIL's lack of accuracy in predicting the boundary layer thickness at the serrated trailing edge.

It has been shown by both Gruber [73] and Chong and Vathylakis [74] that the TBL thickness, for a TE with serrated flat plate extensions, is not equal to that of a straight flat plate extension across a single sawtooth, i.e., δ varies in the spanwise direction as a result

of the serrations. The distribution and development of the TBL across a serration is still debated, and has not yet been modeled. Therefore, without having experimental data specifically defining the TBL for all cases and geometries, using either XFOIL, or Eqn. (2.15), for calculating δ will introduce errors of unknown magnitude. The selection of Eqn. (2.15) is therefore based on its simplicity, computational efficiency, and minimal overhead required for incorporation into the optimization program. An additional advantage of using Eqn. (2.15) is the simplicity of changing the optimization program if a more accurate model is developed for δ across a serration. In such a case, the adjustment would be achieved by replacing the single line of code where δ is calculated using Eqn. (2.15) with the equation of the new model.

Chapter 3

NUMERICAL OPTIMIZATION

This chapter presents the numerical and computational methods used in this work, specifically for the development of the in-house optimization code. The optimization problems are defined first. The in-house optimization program SAGRGSTEN, developed by the author, is then discussed. The optimization algorithm selection is presented and justified, followed by a summary of the program's structure, and logic. The final sections of this chapter are devoted to other numerical methods of importance used in this work.

3.1 Definition of the Optimization Problems

This thesis examines four different optimization problems, which are given below in proper form [75] in Eqns. (3.1) to (3.4). Equations (3.1) and (3.2) correspond to the single-size optimization of sawtooth (see Figure 2.1b), and slitted (see Figure 2.1c) TE geometries, respectively. In each case, the optimum design is the single-size of serration that produces the least amount of total noise over all frequencies between 20 Hz and 20,000 Hz (corresponding to the ideal human hearing range). Results of single-size optimization

studies, defined by Eqns. (3.1) and (3.2), are presented in Section 4.1. Equations (3.3) and (3.4) correspond to the frequency-dependent optimization of sawtooth and slitted TE geometries, respectively. In each of these two cases, an optimum serration design is found at all individual frequencies between 20 Hz and 20,000 Hz. Results of frequency-dependent optimization studies, defined by Eqns. (3.3) and (3.4), are presented in Section 4.3.

$$\begin{aligned}
& \underset{h, \lambda}{\text{minimize}} && Z = \text{OASPL}_{\text{saw}}(h, \lambda) \\
& \text{subject to} && 0 \leq h \leq h_{\text{max}} \\
& && \lambda_{\text{min}} \leq \lambda \leq \lambda_{\text{max}}
\end{aligned} \tag{3.1}$$

$$\begin{aligned}
& \underset{h, \lambda_1, \lambda_2}{\text{minimize}} && Z = \text{OASPL}_{\text{slit}}(h, \lambda_1, \lambda_2) \\
& \text{subject to} && 0 \leq h \leq h_{\text{max}} \\
& && (\lambda_1)_{\text{min}} \leq \lambda_1 \leq (\lambda_1)_{\text{max}} \\
& && (\lambda_2)_{\text{min}} \leq \lambda_2 \leq (\lambda_2)_{\text{max}}
\end{aligned} \tag{3.2}$$

$$\begin{aligned}
& \underset{h, \lambda}{\text{minimize}} && Z = \psi(\omega)_{\text{saw}}(h, \lambda) \\
& \text{subject to} && 0 \leq h \leq h_{\text{max}} \\
& && \lambda_{\text{min}} \leq \lambda \leq \lambda_{\text{max}}
\end{aligned} \tag{3.3}$$

$$\begin{aligned}
& \underset{h, \lambda_1, \lambda_2}{\text{minimize}} && Z = \psi(\omega)_{\text{slit}}(h, \lambda_1, \lambda_2) \\
& \text{subject to} && 0 \leq h \leq h_{\text{max}} \\
& && (\lambda_1)_{\text{min}} \leq \lambda_1 \leq (\lambda_1)_{\text{max}} \\
& && (\lambda_2)_{\text{min}} \leq \lambda_2 \leq (\lambda_2)_{\text{max}}
\end{aligned} \tag{3.4}$$

where Z is the objective function value; h_{max} is the largest feasible serration amplitude (corresponding to the sawtooth and slit geometries accordingly); λ_{min} and λ_{max} are the

smallest and largest feasible sawtooth widths, respectively; $(\lambda_1)_{\min}$ and $(\lambda_1)_{\max}$ are the smallest and largest feasible slit widths, respectively; and $(\lambda_2)_{\min}$ and $(\lambda_2)_{\max}$ are the smallest and largest feasible gap widths, respectively.

3.2 Development of the Optimization Program

3.2.1 Algorithm Selection and Justification

To allow for the selection of the most appropriate optimization technique for the problems studied in this thesis, a number of different techniques were considered and evaluated during the development of SAGRSTEN. Numerical optimization algorithms have been developed since the invention of the digital computer, and new algorithms are developed all the time. There is now an enormous pool of algorithms to choose from, and there are often many algorithms that can solve the same optimization problem. To simplify the selection, an initial screening of algorithms was conducted, thus eliminating ones that are not suitable for this application. The screening conditions correspond to the requirements of the problems defined in Eqns. (3.1) to (3.4). Considerations were also given to potential future optimization studies of TBL-TE noise reduction (see Section 5.3.1). From a thorough examination of the optimization problems, the following conditions were established:

- (i) Computationally efficient;
- (ii) Able to handle both constraints and design variable limits;
- (iii) Able to handle both linear and non-linear objective functions;

- (iv) Only feasible designs (as defined by constraints and design variable limits) should be returned as potential designs;
- (v) Able to discern conditions of optimality from optimization process.

A summary of the algorithms that were screened to meet these conditions is given in the discussion that follows.

Gradient free optimization methods have become very popular over the last decade and are often considered generally superior to traditional, gradient based methods [76]. Algorithms of this type typically employ stochastic strategies for initial design selections and then proceed, using a variety of different logic techniques, to filter out poor designs from the best ones. The process is refined with each subsequent iteration until convergence on the optimum is achieved. The key attribute of these methods is that they do not require evaluation of any derivatives; only the objective function is calculated at each design point. The benefit of not calculating the derivatives is that there is a significant reduction in the number of function evaluations required per iteration, which can theoretically lead to substantial improvements in efficiency. In practice, however, most gradient free algorithms limit the realizable improvement by either evaluating a large number of design points per iteration or, taking many iterations to achieve convergence. Additionally, without calculating the derivatives and using them to navigate the design space, nearly all information defining the objective function's behavior is lost. Often this is of no consequence to the user as convergence on the optimum is still achieved and is typically done at reduced computational time and costs. The sacrifice of this information becomes a significant trade-off if more than just a definition of the optimum point is desired by the user. Without gradients to help guide and traverse a continuous path to extremums, it is

difficult to analyze and develop meaningful conditions of optimality [77]. Gradient-free methods were therefore ruled out as a viable option for the main algorithm as condition (v) is not met.

The two most appropriate gradient-based methods were found to be the generalized reduced gradient (GRG) algorithm and the sequential quadratic programming (SQP) algorithm [75-83]. The main difference between the GRG and SQP algorithms is in how they handle constraints and variable bounds. As previously stated, when the GRG algorithm encounters a bound or constraint, the search direction is adjusted to follow, but never violate it; therefore, the design feasibility condition is always maintained. Conversely, the SQP algorithm gradually enforces feasibility as improvements are made to the objective function, and the only design point that is guaranteed to be feasible is the optimum one [80].

The issues that result from SQP's constraint method are twofold. First, if the optimization is aborted/fails before reaching the optimum, it is entirely possible that no feasible designs exist among the improved designs found. Second, a more serious issue occurs when the domain of the objective function is finite. In this case, SQP will not be strictly limited to design variable values that satisfy the bounds defined by the objective function's domain. It is therefore possible for the algorithm to attempt to evaluate the objective function at design variable values for which no solution exists. Both of these issues are undesirable; however, the latter may cause the entire optimization routine to crash unexpectedly, and, unless a workaround can be used for the objective function definition, may prevent solution using an SQP-based program. This is a prime example to

demonstrate the importance of thoroughly examining the models and equations used to form an objective function [77].

The optimization problems in this thesis are affected by both of the aforementioned SQP issues. For example, the lower bound on λ in Eqn. (3.1) represents the physical limitation in manufacturing; therefore, a design that violates this bound (which may result from pre-mature termination of SQP) is of little use if the limit cannot be relaxed. Additionally, from examination of Eqn. (2.11) it can be seen that the objective function domain is finite. Setting the value of λ to zero produces a singularity, which would result in an error if the solver attempted evaluation at this point, potentially crashing the software. The SQP algorithm was eliminated as a viable choice primarily due to these two issues; however, other factors also influenced this decision.

One additional factor is that the GRG algorithm is fairly simple and intuitive to implement and use relative to the SQP algorithm. Additionally, being one of the most popular nonlinear optimization methods, it is well known, extensively tested, and there are many resources available for it. Consideration was also given to comparisons discussed throughout relevant and important optimization literature, which identified the GRG algorithm as being highly robust. In particular, the results of studies conducted by Sandgren and Ragsdell [82] and Schittkowski [83] were closely examined. Both studies systematically tested numerous nonlinear algorithms on a variety of different problems, and ranked the algorithms by performance. Schittkowski found that three of the top four algorithms were based on the GRG method. Further, Sandgren and Ragsdell found the GRG method to be, by far, the most robust and efficient compared to the other 23 different methods tested.

For the reasons outlined above, the GRG algorithm was chosen for the primary optimization process in SAGRSTEN. The one major limitation of the standard GRG algorithm, however, is its inability to distinguish the global optimum point from local optimum points. This limitation is not unique to the GRG algorithm. Finding and identifying the global optimum for non-convex, nonlinear objective functions is still an evolving field of research. The general approach to use the GRG algorithm (or any gradient-based method) for finding a global optimum is to find the local optimums first and then examine the set to identify the global optimum [81]. The set of local optimums can be found by starting the algorithm from various different starting points throughout the design space [77]. The simplest and most common way to implement this is with a grid search. In the grid search method a set of starting points is generated, in which the members are equally spaced throughout the feasible range of each design variable. The GRG algorithm is then initiated from each starting point in the set sequentially. For every starting point, the algorithm obtains a local optimum. This set of local optimums can then be scanned to find the one with the smallest objective function (or largest for maximization), which is then identified as the global optimum.

The basic grid search method is an improvement on the standard GRG algorithm, and, for a small enough grid spacing, this method will find the global optimum. In practice, however, as the grid spacing is reduced, the computational time required for convergence increases rapidly. Further, the appropriate grid size can only be found by trial and error (i.e. a convergence study of decreasing the grid size), and, due to practical limitations, the global optimum cannot be guaranteed. An optimization problem with many design variables and/or a large/infinite design space would require an impractical amount of computational

time to use this method for finding the global optimum. In order to avoid this efficiency issue a new hybrid method of finding the global optimum using the GRG algorithm is developed by the author and implemented in this thesis.

It was stated early in this section that derivative-free methods were rejected because it is difficult to identify conditions of optimality when using them. One of their most attractive features, however, is their ability to find the global optimum. In particular, probabilistic methods are commonly used to find global optimums because they are able to avoid becoming stuck in local optimums [79]. In a novel attempt to improve the ability of the GRG algorithm to find the global optimum efficiently, while still retaining information needed to define conditions of optimality, a probabilistic/derivative based hybrid method was developed. The method is a combination of the simulated annealing (SA) algorithm and the GRG algorithm. Similar to the grid search, this hybrid method is also based on initiating the GRG algorithm from various starting points throughout the design space. The method selects the starting points using the SA algorithm, in which the design variables are the starting point values of the GRG design variables, and the objective function value is the local minimum found by each execution of the GRG routine. Although this particular combination of algorithms is new, a number of different hybrid optimization methods that combine a probabilistic algorithm with a derivative-based algorithm have been developed in recent years with much success [84-86].

3.2.2 General Structure of the Optimization Program

SAGRGSTEN follows the logic depicted in Figure 3.1 to optimize trailing edge serrations for TBL-TE noise reduction. The program uses the generalized reduced gradient algorithm to search through the design variables for local optimums. The starting points,

from which the GRG algorithm search begins, are chosen with the simulated annealing algorithm. The SA algorithm is also used to establish when a global optimum has been found.

SAGRSTEN functions in two main processes according to the algorithm governing the modification of the design variables. In Figure 3.1, the processes are outlined in dashed gray lines to indicate logic belonging to the SA process (dark gray), and the GRG process (light gray). The program is initiated when the user has defined the optimization parameters and elected to run a study. The user-defined parameters are then sent to the program and the SA process selects a starting point, which is sent to the GRG process. Beginning from this starting point, the GRG process explores the design space until a local optimum is found. The method of exploration is based on a steepest descent line search, in which the search direction is updated when/if a constraint is encountered. Once a local optimum has been found, the point is returned to the SA process. At this point, if the SA algorithm is considered to have converged, the global optimum has been found, the result is displayed to the user and the program is terminated. If the SA algorithm has not yet converged, the current point in the SA process is updated with the newly found local optimum. The updated current point is then perturbed according to the SA algorithm, and a new GRG starting point is established. The program will cycle between the GRG and SA processes in this fashion until the SA algorithm has converged. A more detailed description of the SA and GRG algorithms are given in Section 3.2.3 and 3.2.4, respectively.

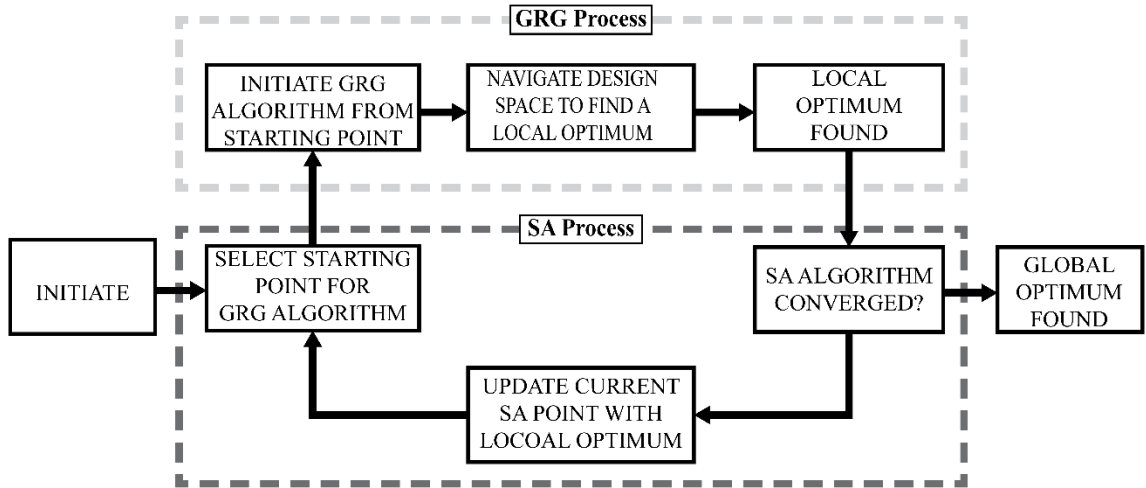


Figure 3.1: Descriptive program flow chart for SAGRSTEN.

3.2.3 SA Algorithm

The SA algorithm mimics the natural process of annealing solids. The annealing process occurs when a very hot solid, currently in its liquid state, is cooled slowly and steadily such that thermal equilibrium is maintained. At the beginning of the process, the solid has a very large amount of energy, but as the temperature is decreased, so too is the energy until some minimum level is reached. This process is implemented into a numerical algorithm through representing the system's 'energy' by the objective function. At the start of the algorithm, the objective function value is very large. As the algorithm progresses, the objective function value is reduced until the minimum is reached [76-78].

In the first SA iteration, the design variable values are randomly selected, and the objective function is calculated at this point. The design variables are then perturbed by a small amount and the objective function is calculated again at this new perturbed point. If the value of the objective function at the perturbed point is less than the un-perturbed objective function value (i.e., the energy, E , has decreased), then the perturbed point is automatically accepted as the new design point (from which the next perturbation will

expand from). If the energy of the perturbed state has increased, the perturbed point will have a certain probability of acceptance, \wp , and a complimentary probability of rejection, $(1-\wp)$. The probability of accepting a point with greater energy is determined according to the Metropolis criterion, which uses the Boltzmann probability distribution [87]:

$$\wp(E_{n+1}) = \exp\left[-\frac{E_{n+1} - E_n}{k_b T}\right] \quad (3.5)$$

where k_b is the Boltzmann constant, which serves as a scaling factor, but is typically chosen as 1 for simplicity, and T is the temperature at the current iteration. Equation (3.8) defines the mechanism that allows the SA algorithm to “climb hills”, and outlines the conditions where choosing one (or several) increases in the objective function may actually lead to smaller minimum values and even the global minimum. As the algorithm progresses and the temperature is decreased, the probability that an increased energy level point will be accepted decreases exponentially. In addition, for any temperature, T , the probability, \wp , decreases with increasing change in energy, i.e., a point with a small to moderate increase in energy has a greater chance of acceptance than a point with a large increase in energy. When the objective function value has not changed within a certain number of iterations, or T reaches some final equilibrium value, the SA algorithm is said to have converged on the minimum objective function value and associated design variable values.

In SAGRSTEN, the SA algorithm controls the global optimization loop by generating starting points, calling the GRG process, and identifying the global optimum. Initially, the first starting point is chosen by generating a random number between the upper and lower bounds of each variable. This point is then sent to the GRG process to obtain the initial local optimum value. From here, the iterative SA loop begins in which the current point is perturbed, the new local optimum value is obtained from the GRG process, and the

perturbed point is either accepted or rejected as the new current point according to Eqn. (3.5). After each SA iteration, the temperature is reduced according to:

$$T = \left(\frac{T_f}{T_0}\right)^{1/(N-1)} T \quad (3.6)$$

where T_0 and T_f are the initial and final temperatures, respectively, and N is the maximum number of SA iterations.

The program continues in this fashion until either the current local optimum value has not changed for the user-defined number of SA iterations, or the SA temperature has fallen below a user-defined value. If either of these conditions is true, the current local optimum point is the global optimum and the SA algorithm is terminated.

3.2.4 GRG Algorithm

The main sequence of logic used by the optimization program to find local optimums follows the Generalized Reduced Gradient algorithm. The GRG algorithm is a particular implementation of the quasi-Newton optimization method [77]. It is a gradient-based numerical optimization algorithm that is capable of finding optimum points for linear and non-linear design problems that are either constrained or unconstrained. Starting with initial, feasible values of the design variables, the main process of the GRG algorithm is to move in the direction of steepest descent until either

- (i) An optimum point is found, or for a constrained problem,
- (ii) A constraint/variable bound is encountered.

In the case of (ii), the algorithm then modifies the search direction to follow the constraint/variable bound as the descent continues. This process of finding and following

design boundaries throughout the descent is continued until an optimum point is found [77].

The specific implementation of the GRG algorithm in SAGRSTEN is based on the logic of Lasdon's GRG2 optimization program [88, 89]. GRG2 was chosen as a basis for development because it is the most widely distributed and publicly available implementation of the GRG algorithm. Additionally, it is used as the optimizer in foundational software programs like Microsoft Excel and Novell's Quattro Pro among others [80]. An overview of the GRG2 implementation is given here; however, the reader is directed to Ref. [88] and [89] for the specifics of Lasdon's program.

First, the constraint and objective function values, as well as their partial derivatives, with respect to the design and slack variables, are calculated. The slack variables are a numerical construct added to inequality constraint equations in order to convert them into equalities. This slack variable mechanism allows the algorithm to both quantify the current point's proximity to constraints, and make one or more constraint binding (such that the path of descent will be incident to the constraint) [77].

After checking the constraints and variable bounds for violations, the variables are partitioned and the basis is constructed. This is done by first partitioning the variables into basic, \mathbf{X}_b , and nonbasic, \mathbf{X}_{nb} , variables and then forming the basis matrix, \mathbf{B} , according to Eqn. (3.7):

$$\mathbf{B} = \begin{bmatrix} \frac{\partial g_1}{\partial X_{b_1}} & \dots & \frac{\partial g_1}{\partial X_{b_{m_{bc}}}} \\ \vdots & \ddots & \vdots \\ \frac{\partial g_{m_{bc}}}{\partial X_{b_1}} & \dots & \frac{\partial g_{m_{bc}}}{\partial X_{b_{m_{bc}}}} \end{bmatrix} \quad (3.7)$$

where g_i is the i^{th} binding constraint and m_{bc} is the number of currently binding constraints. \mathbf{X}_{nb} is a vector that is always of size m_{dv} , the total number of design variables, and will contain $(m_{dv} - m_{bc})$ design variables and m_{bc} slack variables; \mathbf{X}_b is a vector of size m_{bc} that contains only design (non-slack) variables. \mathbf{B} is a square matrix of size m_{bc} -by- m_{bc} and is constructed from the partial derivatives of the active constraints with respect to the basic variables.

Using the partial derivatives and the basis matrix, the reduced gradient, $\nabla \mathbf{F}_R$, is calculated as:

$$\nabla \mathbf{F}_R = \left(\frac{\partial Z}{\partial \mathbf{X}_{nb}} \right) - \left(\frac{\partial Z}{\partial \mathbf{X}_b} \right)^T (\mathbf{B}^{-1}) \left(\frac{\partial \mathbf{g}}{\partial \mathbf{X}_{nb}} \right) \quad (3.8)$$

Before using $\nabla \mathbf{F}_R$ to calculate the new search direction, the current design point is evaluated for optimality. The point is considered an optimum if either of the following two conditions is met:

- (i) All non-basic variables satisfy one of the following conditions:
 - a. $X_{nb_i} = LB_i$ and $\nabla F_{R_i} \geq -e_{\text{stop}}$
 - b. $X_{nb_i} = UB_i$ and $\nabla F_{R_i} \leq e_{\text{stop}}$
 - c. $LB_i < X_{nb_i} < UB_i$ and $|\nabla F_{R_i}| < e_{\text{stop}}$
- (ii) $|Z - Z_0| < e_{\text{stop}}|Z_0|$ for 10 consecutive iterations

where LB_i and UB_i are the lower and upper bounds, respectively, on the i^{th} non-basic variable; e_{stop} is the user defined numerical tolerance, which has a default value of 10^{-4} ; and $|Z_0|$ is the absolute value of the objective function at the previous GRG iteration. Condition (i) defines the Kuhn-Tucker conditions for optimality, and condition (ii) is a secondary test to avoid the algorithm from becoming stuck. If either condition is satisfied,

the GRG algorithm is terminated, and the local optimum point is returned to the SA algorithm. If neither condition is satisfied, the new search direction is calculated from the reduced gradient, using the Broyden–Fletcher–Goldfarb–Shanno (BFGS) update method, and the one dimensional line search is initiated. The BFGS update is a method of approximating the Hessian matrix, and has the desirable attribute that each updated search direction is guaranteed to be positive definite [76, 79]. When the search terminates, the constraint, objective function, and partial derivatives are calculated, and the next GRG iteration begins.

3.3 Additional Numerical Methods

3.3.1 Calculation of the Objective Function

The OASPL used for the objective function in the optimization problems of Eqns. (3.1) and (3.2) is defined by Eqn. (2.14). To compute the integral in this equation analytically, however, would be extremely cumbersome and highly problem specific. In order to maintain ease-of-use and robustness of the optimization program, Eqn. (2.14) was converted into a numerical integration. The numerical integration is calculated using the Trapezoidal method via the built-in MATLAB function *trapz*. The *trapz* function performs numerical integration using the following discrete summation formula:

$$\int_{\omega_{\min}}^{\omega_{\max}} \psi(\omega) d\omega = \frac{1}{2} \sum_{n=1}^N [\omega_{n+1} - \omega_n] [\psi(\omega_n) + \psi(\omega_{n+1})]. \quad (3.9)$$

For the GRG algorithm, and most other optimization algorithms, there is a strong potential for the existence of significant numerical error if the variables and objective

function are either very small or large relative to each other. The error is a result of the limitation in precision during numerical operations performed by a digital computer. A common practice to avoid this error, without restricting user input, is to include a scaling process in the optimization program [75, 77]. The scaling process adjusts the values of the variables and objective function such that they all fall within one order of magnitude of each other. In SAGRGSTEN, the scaling process is done immediately following calculation of the objective function value. The objective function value was scaled as follows:

$$Z_{sc} = \frac{(Z - \tilde{Z}_{min})}{(\tilde{Z}_{max} - \tilde{Z}_{min})} |DV|_{max} \quad (3.10)$$

where Z_{sc} is the scaled objective function value; Z is the un-modified objective function value from any of Eqns. (3.1) to (3.4); \tilde{Z}_{min} and \tilde{Z}_{max} are the approximate minimum and maximum values, respectively, of Z throughout the entire feasible design space; and $|DV|_{max}$ is the absolute maximum value of all design variables. \tilde{Z}_{min} , \tilde{Z}_{max} , and $|DV|_{max}$ are all calculated in the initialization phase, before entering the global optimization loop, and are kept constant throughout each optimization study. The approximation for the minimum and maximum values of Z is done by searching through a set of distributed objective function values. The set is formed by calculating the objective function at six, evenly spaced, values of each design variable distributed between the associated lower and upper limits (including one at each limit). This process gives 6^n number of Z values (where n is the total number of design variables) throughout the design space, to be filtered sequentially for the approximate minimum and maximum values. While using a grid as course as this to mesh the design space does not provide a satisfactory resolution for an

optimization search, it does yield reasonable approximations to the extremums of Z (i.e., within one order of magnitude) for the scaling process in SAGRGSTEN.

3.3.2 Calculation of the Numerical Derivatives

The primary method used in SAGRGSTEN for calculating the partial derivatives numerically is the second order, central difference formula, given in Eqn. (3.11). This method was chosen for its balance between calculation speed and accuracy as compared to, for example, the first order, forward difference formula or the fourth order, central difference formula [81]. An additional benefit of central differencing methods is that they equally consider the function's behaviour from both a positive and negative perturbation.

$$\frac{\partial Z}{\partial DV_i} = \frac{Z(DV_i + \xi) - Z(DV_i - \xi)}{2\xi} + O(\xi^2) \quad (3.11)$$

In the particular case where the design variable, DV_i , is less than or equal to the step size, ξ , Eqn. (3.11) cannot be used as Eqns. (2.11) and (2.12) are not valid in this range, and the resulting derivative value(s) may produce an incorrect search direction. To avoid this issue, without sacrificing the level of accuracy given by Eqn. (3.11), the 2nd order, three-point, forward difference formula, Eqn. (3.12), is used instead [90]. As indicated by the name, it is also 2nd order accurate; however, no perturbations in the negative direction are required thus allowing for a valid calculation of the derivative for all values of DV_i greater than zero. A three-point finite difference method requires three values of the function instead of only the two used in Eqn. (3.11), which suggests a slower speed of calculation. In the SAGRGSTEN program, however, the objective function at the current point, $Z(DV)$, is calculated for every call to the function where the derivative calculation is

done. This means that both finite difference methods require the same number of function calls and therefore have equal calculation speed.

$$\frac{dZ}{dDV_i} = \frac{[-3Z(DV_i) + 4Z(DV_i + \xi) - Z(DV_i + 2\xi)]}{2\xi} + O(\xi^2) \quad (3.12)$$

These finite difference methods are 2nd order accurate as their derivation is based on Taylor expansions up to the quadratic term, i.e., 2nd order Taylor series [91]. In both Eqns. (3.11) and (3.12), the accuracy is indicated using ‘big-*O*’ notation and it is readily seen that the error is quadratically dependent on the step size, therefore suggesting that error is reduced by minimizing ξ . It is generally true that using a smaller step size will produce less error; however, this is only indicative of the truncation error (error resulting from using a finite number of terms from an infinite Taylor series). Digital computing also introduces round-off error as a result of approximating exact, real decimal numbers to floating point form with a finite number of digits. The round-off error increases significantly from mathematical operations between two numbers of very different magnitude, i.e., division by a very small step size. It then follows that, instead of using the smallest value possible for ξ , there exists some optimum value, $\xi^* > \xi_{\min}$, that minimizes the total numerical error. This optimum value can be derived by approximating both the round-off and truncation error by their upper bounds and summing them together. The upper bound of the truncation error cannot be found practically, but an approximation for ξ^* in a 2nd order finite difference equation is given by Kopecky [90] as follows:

$$\xi^* \approx |DV_i| \epsilon^{1/3} \quad (3.13)$$

where ϵ is the machine epsilon term, which for double precision computing is approximated as $\epsilon^{1/3} \approx 10^{-6}$ (based on $\epsilon = 2.22 \times 10^{-16}$).

Chapter 4

RESULTS AND DISCUSSION

This chapter first presents the results of the optimization studies in which the objectives are to minimize the TBL-TE noise by introducing flat-plate trailing edge serrations. First, the serrations are optimized to find the single size of each tooth geometry (sawtooth and then slitted) that produces the least noise over the entire frequency spectrum of interest (20 Hz to 20 kHz), for each set of constraints examined. Then, the serrations are optimized at individual frequencies to find the size of each tooth geometry that produces the least noise at each of the 10,000 logarithmically spaced frequencies between 20 Hz and 20 kHz.

Throughout all of the optimization studies the parameters in Eqns. (2.10) to (2.13) (which are part of the objective function definitions) pertaining to fluid flow (δ , and U_c) are kept constant, while the geometrical parameters (h , λ , λ_1 , λ_2) are the design variables and are therefore manipulated by SAGRSTEN to find the minimum point. The mean flow speed was chosen to be 40 m/s as this is representative of aircraft landing conditions, and it is equal/near the flow speed used in many experimental studies published in the literature [46, 47, 74, 92]. Based on this mean flow speed U_c is 28 m/s, δ is approximately 4 mm (as calculated using methods described in Section 2.3.2), the Mach number is 0.17 and the

Reynolds number is approximately 4.8×10^5 (based on air density of 1.28 kg/m^3 , and dynamic viscosity of $1.72 \times 10^{-5} \text{ kg/m}\cdot\text{s}$) [70].

A summary of the optimization study settings is given in Table 4.1. The single size sawtooth and slitted optimization studies are labeled as SS-Saw and SS-Slit, respectively. The individual frequency, or frequency-dependent, optimizations of sawtooth and slitted serrations are labeled as FD-Saw and FD-Slit, respectively.

Table 4.1: Optimization trials and associated design variable bounds

Study No.	Bandwidth	Lower DV Bounds [mm]			Upper DV Bounds [mm]		
		λ_1	λ_2	h	λ_1	λ_2	h
SS-Saw-1	Broad	1	-	0	17.5	-	δ
SS-Saw-2	Broad	0.5	-	0	17.5	-	15
SS-Saw-3	Broad	0.1	-	0	17.5	-	15
SS-Saw-4	Broad	0.5	-	0	17.5	-	30
SS-Saw-5	Broad	0.1	-	0	17.5	-	30
SS-Slit-1	Broad	0.5	0.5	0	20	20	15
SS-Slit-2	Broad	0.5	0.1	0	20	40	15
SS-Slit-3	Broad	0.1	0.1	0	40	40	30
FD-Saw-1	Narrow	0.1	-	0	40	-	30
FD-Saw-2	Narrow	0.5	-	0	20	-	15
FD-Saw-3	Narrow	0.5	-	0	20	-	30
FD-Saw-4	Narrow	0.1	-	0	40	-	15
FD-Slit-1	Narrow	0.1	0.1	0	40	40	15
FD-Slit-2	Narrow	0.5	0.5	0	20	20	15
FD-Slit-3	Narrow	0.1	0.1	0	40	40	30
FD-Slit-4	Narrow	0.5	0.5	0	20	20	30

The optimized designs from each study, and their respective OASPLs, are given in Table 4.2. Additionally, the OASPL for a straight trailing edge is given in the last row of the table for comparison. The h_{opt} column, for the frequency-dependent sawtooth and slitted optimization studies, contains the variable $h_{\text{opt}}(f)$ instead of actual numerical values.

This variable is used to indicate that there is no single optimum value, and that the optimum value of the serration amplitude is a continuous function of frequency for the respective study. For the specific h_{opt} function and associated conditions, the reader is directed to Sections 4.3.1 and 4.3.2 for the frequency-dependent sawtooth and slitted trailing edge optimization studies, respectively.

Table 4.2: Optimized designs from each study and noise produced by each trailing edge

Study No.	Optimal Geometry [mm]			OASPL [dB]
	$(\lambda_1)_{\text{opt}}$	$(\lambda_2)_{\text{opt}}$	h_{opt}	
SS-Saw-1	1	-	δ	29.504
SS-Saw-2	0.5	-	15	19.300
SS-Saw-3	0.1	-	15	19.209
SS-Saw-4	0.5	-	30	13.377
SS-Saw-5	0.1	-	30	13.194
SS-Slit-1	0.5	0.5	3.259	32.197
SS-Slit-2	0.5	0.1	3.272	34.067
SS-Slit-3	0.1	0.1	3.275	32.015
FD-Saw-1	0.1	-	$h_{\text{opt}}(f)$	9.022
FD-Saw-2	0.5	-	$h_{\text{opt}}(f)$	17.599
FD-Saw-3	0.5	-	$h_{\text{opt}}(f)$	9.688
FD-Saw-4	0.1	-	$h_{\text{opt}}(f)$	17.397
FD-Slit-1	0.1	0.1	$h_{\text{opt}}(f)$	12.177
FD-Slit-2	0.5	0.5	$h_{\text{opt}}(f)$	21.671
FD-Slit-3	0.1	0.1	$h_{\text{opt}}(f)$	8.855
FD-Slit-4	0.5	0.5	$h_{\text{opt}}(f)$	21.429
Straight TE	-	-	-	35.723

4.1 Verification and Validation

4.1.1 Verification of SAGRGSTEN

To ensure that the optimization program SAGRGSTEN functions correctly, the finalized code was thoroughly tested and debugged. Initially, the following test case from Ref. [77] was used:

$$\begin{aligned}
& \underset{x_1, x_2}{\text{minimize}} && Z = x_1^2 + x_2 \\
& \text{subject to} && x_1^2 + x_2^2 - 9 \leq 0 \\
& && x_1 + x_2 - 1 \leq 0
\end{aligned} \tag{4.1}$$

The test problem defined in Eqn. (4.1) is a nonlinear, constrained optimization problem. This problem has a nonlinear objective function with two design variables and two nonlinear inequality constraints. It was chosen specifically because it has a known and definite solution, and it is a good representation of the optimization problems defined in Eqns. (3.1) to (3.4). The design space and constraints of Eqn. (4.1) are given in Figure 4.1 as a contour plot.

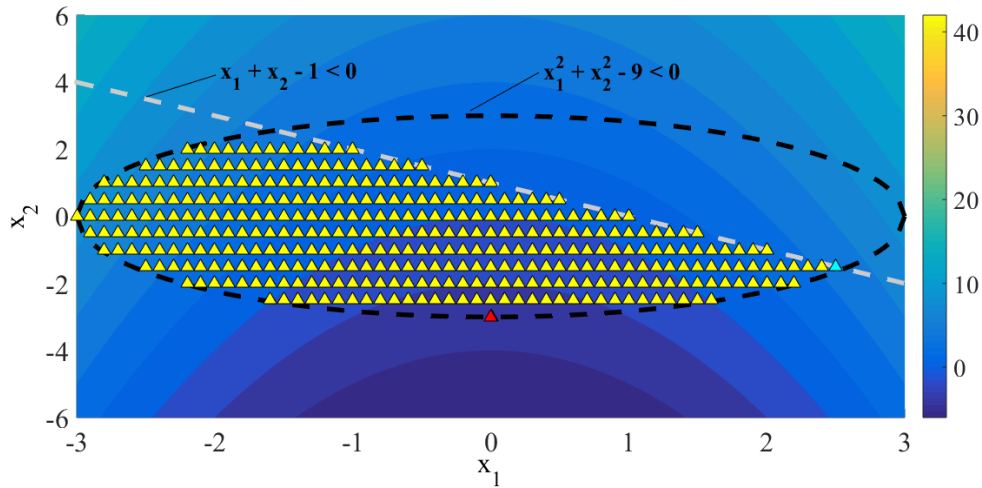


Figure 4.1: Design space plot of test optimization problem defined in Eqn. (4.1) with distribution of starting points (yellow and cyan triangles) and optimum points found (red triangles) shown.

First, the gradient-based local search controlled by the GRG algorithm was verified by starting the optimization routine from the same starting point given as an example in Ref. [77]. This starting point is indicated in Figure 4.1 by the cyan coloured triangle marker located at $x_1 = 2.56155$ and $x_2 = -1.56155$. From this starting point, the optimization routine was manually progressed one step at a time, and checked so that every part of the

GRG algorithm was confirmed to be working properly. The final optimum point found by the local search (indicated by the red coloured triangle marker) was then compared to the solution given in Ref. [77]. Then, the optimization routine was initiated from a number of different starting points that were distributed throughout the design space. The distribution of starting points is indicated by the yellow coloured triangle markers. This process ensured that the implementation of the GRG algorithm was fully functioning throughout the entire design space, and therefore in the full range of applicable scenarios required by Eqns. (3.1) to (3.4).

As a final step in the verification process of SAGRGSTEN, a contour plot of the design space corresponding to Eqn. (3.1) was produced at the start of the program. In a similar fashion to Figure 4.1, the points found at each step in both the SA algorithm, and the GRG algorithm, were plotted on the design space contour plot. After initiation, SAGRGSTEN was progressed manually through each line of code. This process was done for several studies varying the constraints, initial starting point and design space each time. Once the ability of SAGRGSTEN to thoroughly explore the design space of Eqn. (3.1) was rigorously tested, and full functionality was verified, the same procedure was conducted for Eqns. (3.2) to (3.4).

4.1.2 Verification and Validation of Noise Models

The noise models in Eqns. (2.10) to (2.12) were converted into numerical form in custom MATLAB functions to be used for SAGRGSTEN. In order to verify that the MATLAB functions gave correct values for the noise, the function outputs were compared to results published by Howe [45] (for Eqns. (2.10) and (2.11)), and by Azarpeyvand *et al.*

[47] (for Eqn. (2.12)). Based on the thorough comparison in this analysis, it was concluded that the in-house functions give results nearly identical to the analytical equivalents.

The accuracy of Howe's model for predicting TBL-TE noise from a serrated TE has been addressed a number of times throughout relevant literature [45, 46, 48, 74, 93]. A detailed analysis regarding the accuracy of Howe's model is outside the scope of this thesis; however, the general ability to predict measured results was examined for completeness. Howe's model is an idealization of the acoustic wave scattering process, and several simplifying assumptions are made throughout the derivation (see Section 2.2). It is therefore expected that some discrepancies exist between predicted and measured values. For several reasons, including limited/no alternative models and a high computational efficiency, some degree of error between the predicted and measured noise is accepted in this work. A full justification for selecting Howe's model as the noise prediction tool in this thesis is given in Chapter 1.

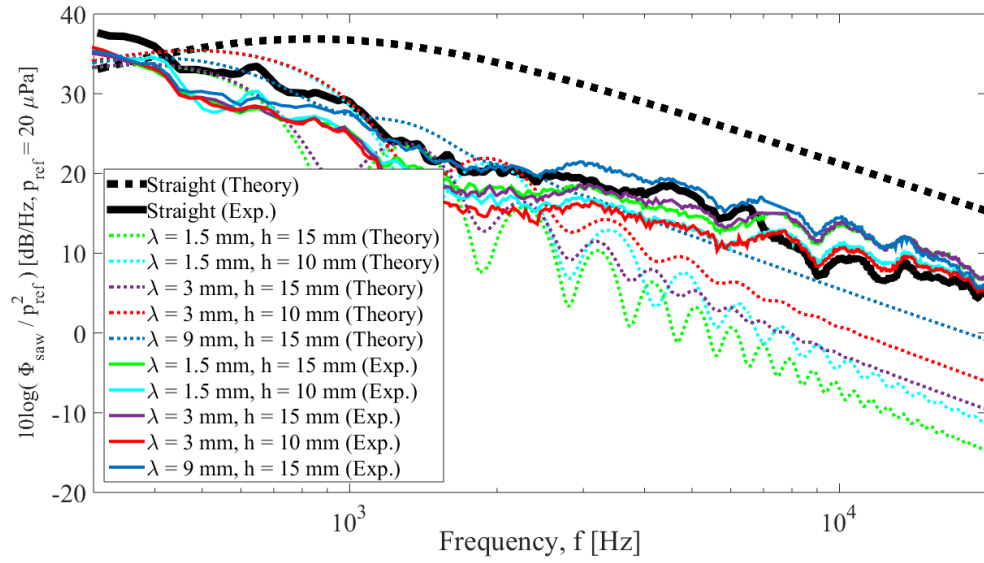


Figure 4.2: SPL frequency spectrum (0.3 to 20 kHz) for straight and sawtooth trailing edges showing a comparison between Howe's model and experimental measurements (extracted from Ref. [46]).

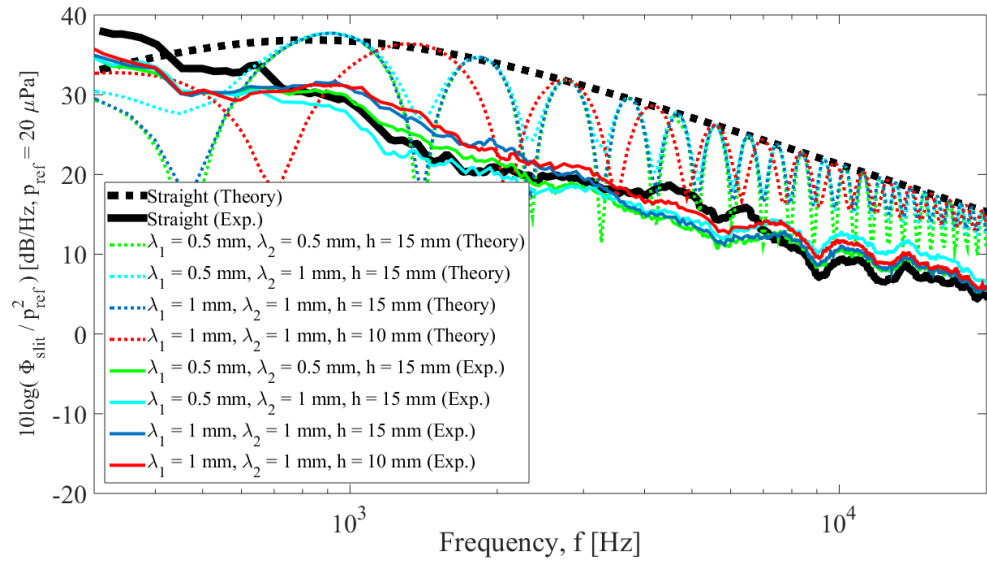


Figure 4.3: SPL frequency spectrum (0.3 to 20 kHz) for straight and slitted trailing edges showing a comparison between Howe's model and experimental measurements (extracted from Ref. [46]).

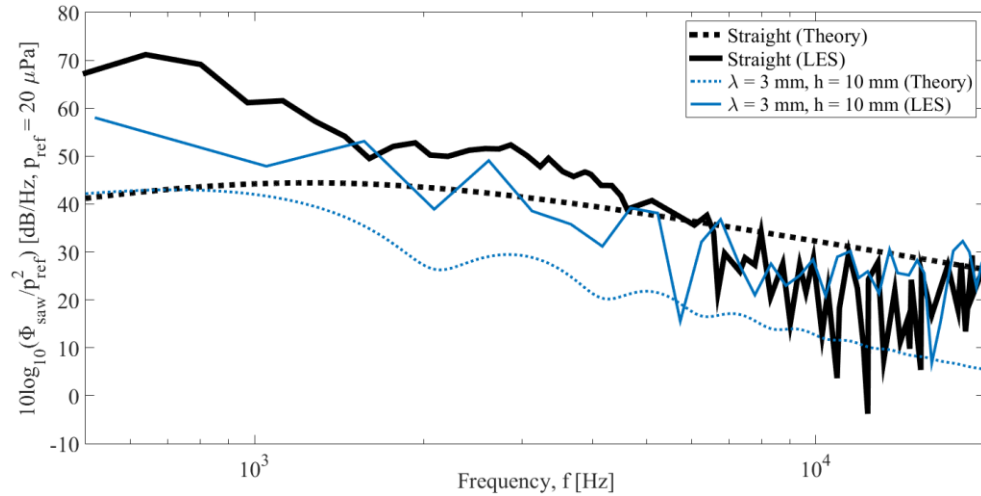


Figure 4.4: SPL frequency spectrum (0.5 to 20 kHz) for straight and sawtooth trailing edges showing a comparison between Howe's model and large eddy simulation results (extracted from Ref. [30]).

An examination of the accuracy of Howe's model was conducted by comparing the predicted noise spectrums to a sample of experimental results published by Gruber *et al.* [46]. The experimental results were obtained in the ISVR's open-jet wind tunnel at a mean flow speed of 40 m/s and were measured using a microphone mounted 90° above the TE at a distance of 1.2 m. The theoretical and extracted experimental SPL results were then plotted for a range of sawtooth sizes in Figure 4.2, and for a range of slit sizes in Figure 4.3. Additionally, theoretical results from Howe's model were also compared to numerical simulation results published by Arina *et al.* [30] (given in Figure 4.4). The results from Ref. [30] were calculated using a compressible large eddy simulation with a free-stream Re of 6.0×10^5 and Mach number of $M = 0.17$. From examination of Figure 4.2, Figure 4.3, and Figure 4.4, it is clearly seen that the SPL spectrums calculated using Howe's model provide reasonable predictions of the experimental SPL spectrums across most frequencies. General trends, such as the mid-to-high frequency decay, are captured by the models, and in some cases, the error between predicted and measured values is less than 1 dB.

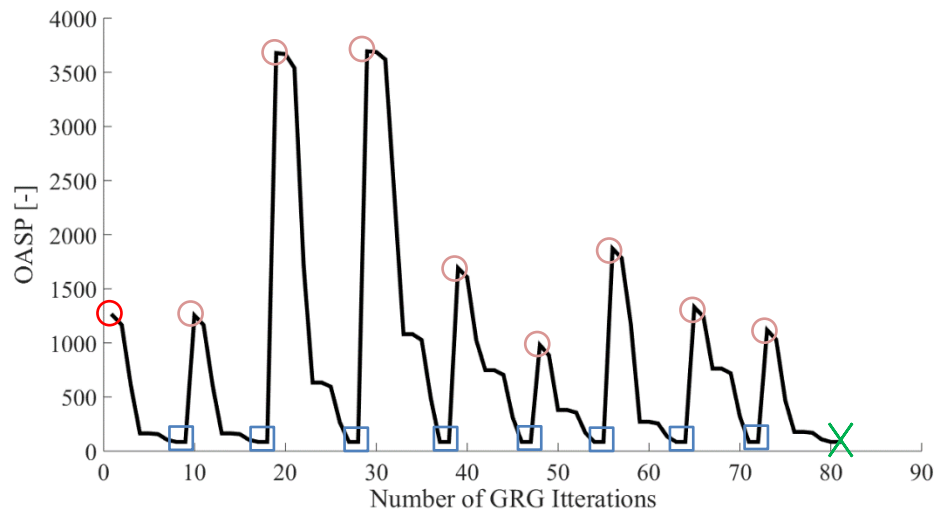
The predicted SPL spectrums are not perfect, however, and some discrepancies exist. The main region of error is observed in the sawtooth SPL spectrum (Figure 4.2) at high frequencies. In this region, the decay rate of the experimental spectrums is seen to level off; however, the decay rate of the predicted spectrums remains constant. Further, near approximately 7 kHz, the measured sawtooth TE spectrums cross over the measured straight TE spectrum. This phenomenon is often referred to as the high-frequency noise increase, and has been observed in a number of experimental studies [46, 74, 93, 94]. Gruber *et al.* [46, 93] studied the high-frequency noise increase, and proposed that the root cause is due to a misalignment between the serrations and the mean flow. Howe's model assumes both that the flow is uniform and strictly in the streamwise direction, and that the serrations are perfectly aligned with the flow [45]. These assumptions explain the discrepancy in the sawtooth SPL spectrums at high frequencies; however, there is currently no method of predicting the noise increase magnitude or frequency dependence. Therefore, the associated error in this region cannot yet be accounted for in the optimization studies.

4.2 Single-Size Serrations

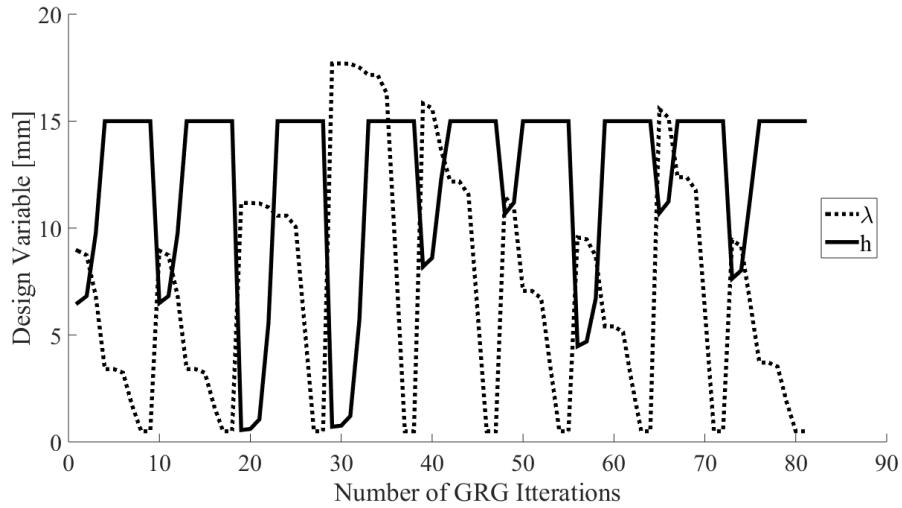
4.2.1 Sawtooth

The SAGRSTEN convergence history is plotted in Figure 4.5 for study SS-Saw-2. From inspection of Figure 4.5, the path of optimization can be seen, in which the design variables (Figure 4.5b) are modified until a local minimum (indicated by the blue squares) in the value of the OASP is found (Figure 4.5a). After finding a local minimum, the design variables jump back to starting values (indicated by the pale red circles), which are

randomly selected by the SA algorithm. In this case, only one local minimum exists, which is found on every SA iteration. Therefore, convergence on the global minimum (indicated by the green X) is achieved after nine SA iterations, which is the default maximum number of loops through the SA algorithm without a change in the objective function value (here being the local minimums found in OASP). Figure 4.5b shows that in each GRG iteration, the greatest improvement is obtained initially by simultaneously increasing h and decreasing λ . The GRG algorithm continues to follow this path until the upper design variable limit on h is encountered. At this point, h is held at its limit of h_{\max} (in this case equal to 15 mm), and λ is driven sharply towards its minimum value. When the algorithm encounters the lower design variable limit on λ , condition (i) of Section 3.2.4 is satisfied for all variables and, therefore, the local optimum is found.



(a)



(b)

Figure 4.5: Optimization study SS-Saw-2 SAGRGSTEN convergence history of (a) the objective function in terms of the OASP, and (b) the sawtooth design variables h and λ

The noise spectrums for both a straight TE and each of the optimized, single-size, sawtooth TE designs are given in Figure 4.6. The straight TE spectrum is seen to increase with frequency up to a maximum value (referred to later as the ‘hump’ in the spectrum) occurring in the mid-frequency range (~ 1.5 kHz), and then decays with increasing frequency in the upper-mid to high frequency range. This shape is a direct result of the turbulence blocked pressure term in Howe’s model (see Eqn. (2.3) for P_b term), and is actually representative of the relative contribution from a turbulent structure (having an associated size and frequency) to the mean square wall pressure [19]. The low frequencies correspond to larger, slower moving turbulent structures, while the high frequencies correspond to the smaller, faster moving ones. The high frequency decay occurs because the energy of smaller, faster structures tends to decay more rapidly in time and space due to viscous fluid forces [18]. The hump in the spectrum corresponds to the convective ridge, which is centered on structures with streamwise wavenumbers of ω/U_c [19]. It is also seen

that, since the same distribution of turbulent energy in the TBL is assumed to occur regardless of the TE geometry, spectrums of all serration designs follow a similar, but not exact, shape to the straight TE (increase, maxima, decay). The deviations between the straight and serrated TE spectrums occur due to a fluid-structure coupling. The energy contained in turbulent structures is scattered into acoustic energy upon interaction with the TE geometry, and oscillations in the spectrum occur because of the correlation between a serration tooth and turbulent structures of particular sizes/frequencies [19].

The optimized single-size sawtooth design, which produced the least noise, was obtained in study SS-Saw-4. This study applied the largest upper limit, and the smallest lower limit on h and λ , respectively compared to the other studies in the SS-Saw group. The OASPL produced by SS-Saw-5 was 13.194 dB, corresponding to a 63.07% reduction in OASPL, compared to a straight trailing edge.

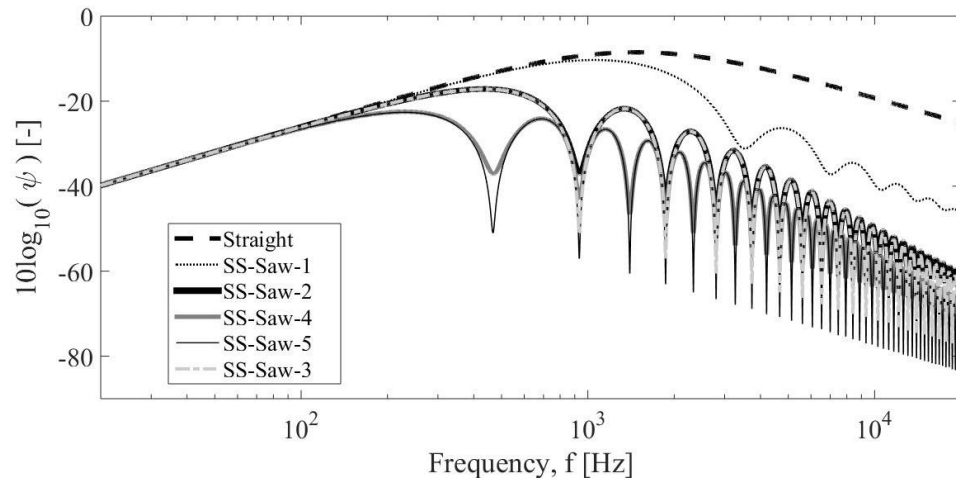


Figure 4.6: SPL plotted as a function of frequency between 20 Hz and 20 kHz for optimum single size sawtooth trailing edge profiles.

The bounds applied in the study SS-Saw-1 represent the range of sawtooth geometries for which Howe presented the original, semi-empirical, noise spectrum results in Ref. [45]. Similarly, the SS-Saw-2 bounds were applied to represent the range of sawtooth

dimensions used in a number of relevant TBL-TE noise studies [46, 92, 93]. These bounds were systematically adjusted for SS-Saw-3, SS-Saw-4, and SS-Saw-5, to investigate the effect of relaxing the bounds on h_{\max} and λ_{\min} , respectively. In each of the four single-size sawtooth optimization studies, the optimum sawtooth geometry coincided with the lower bound on the serration width, λ_{\min} , and the upper bound on the serration amplitude, h_{\max} . This result is in general agreement with the literature, provided that the high-frequency noise increase phenomenon, which has been observed in experimental serrated TE noise measurements [46, 74, 93, 94], is not considered. The specific source of the experimental high-frequency noise increase has yet to be confirmed, and currently no TBL-TE noise models account for it; therefore, proper consideration for its influence on optimum serration design cannot yet be given. Each of the optimum designs in studies SS-Saw-1 to 4 produce a lower OASPL than the straight TE; however, significant variations are seen in the amount of reduction achieved between the four, single-size, sawtooth TE designs. This observation suggests that the optimization process, using SAGRSTEN, is able to produce TE serration designs that produce less noise than designs that have previously been studied, and whose dimensions were chosen manually.

A further investigation into the influence of the sawtooth parameters revealed several relationships. First, as originally observed by Howe [45], and later confirmed experimentally in Ref. [93], the rate of decay in the SPL at high frequencies is dependent on the sawtooth width-to-amplitude ratio, λ/h . As λ/h decreases (i.e., the teeth become more slender), the rate at which the SPL decays in the high frequency range increases. Second, the frequency at which the n^{th} noise reduction peak (sharp SPL drop-offs seen in Figure 4.6) occurs, f_{peak^n} , is dependent on h . This relation is expressed as the following:

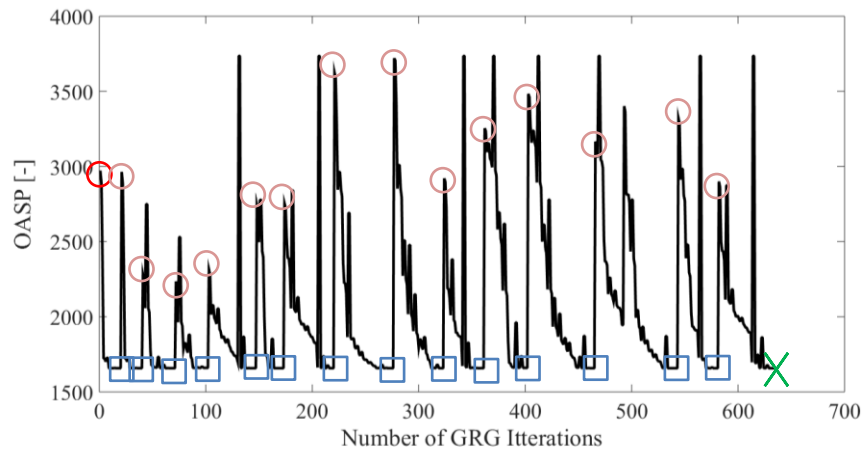
$$f_{\text{peak}}^n = n \left(\frac{U_c}{2h} \right) \text{ for } n = 1, 2, 3, \dots \quad (4.2)$$

It then follows, from Eqn. (4.2), that the first reduction peak, f_{peak}^1 , is given by the ratio $U_c/2h$, which decreases with increasing h , i.e., the first reduction peak occurs at a lower frequency for a longer sawtooth. Further, it is easily seen by inspection of both Figure 4.6, and Eqn. (4.2), that the peak-to-peak frequency bandwidth, Δf_{peak} , is equal to f_{peak}^1 , and is constant across the entire spectrum for a given h value. Gruber *et al.* [46] also found that f_{peak}^n is independent of λ ; however, the expression they obtained for f_{peak}^n differs slightly from Eqn. (4.2), and does not match results presented in this thesis.

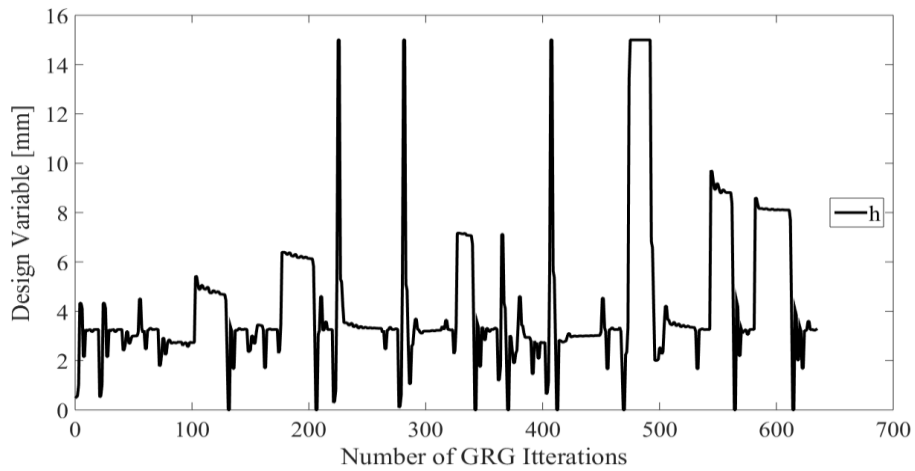
4.2.2 Slitted

The SAGRGSTEN convergence history is plotted in Figure 4.7 for study SS-Slit-1. The path of optimization for a slitted trailing edge is seen to be significantly more erratic than for a sawtooth trailing edge. This is due to several factors, including the additional design variable, the high sensitivity of the OASPL to changes in the design variables, and the global optimum not coinciding at an intersection of design variable limits. As a result, there are very large jumps in the OASPL between when a local optimum (indicated by the blue squares) is found, and the next starting point (indicated by the pale red circles) chosen by the SA algorithm. The erratic optimization path also requires a large number of GRG iterations for each SA iteration, as well as more SA iterations to establish that the global optimum (indicated by the green X) is found. From inspection of Figure 4.7c, it is seen that, throughout each SA iteration, the values of λ_1 and λ_2 oscillate relative to each other. As they converge on their respective minimum values, the oscillation amplitude diminishes, and become equal when they encounter their lower limits. By comparison of

Figure 4.7b to Figure 4.7c, it is seen that the value of h is held relatively constant, at a point close to the starting value, until λ_1 and λ_2 converge on their lower limits. Once the two widths are at their minimum values, the value of h is aggressively adjusted towards the optimum value. This sharp change in h overshoots the optimum value, thus inducing oscillations in h , which are critically damped by the GRG algorithm until convergence is achieved.



(a)



(b)

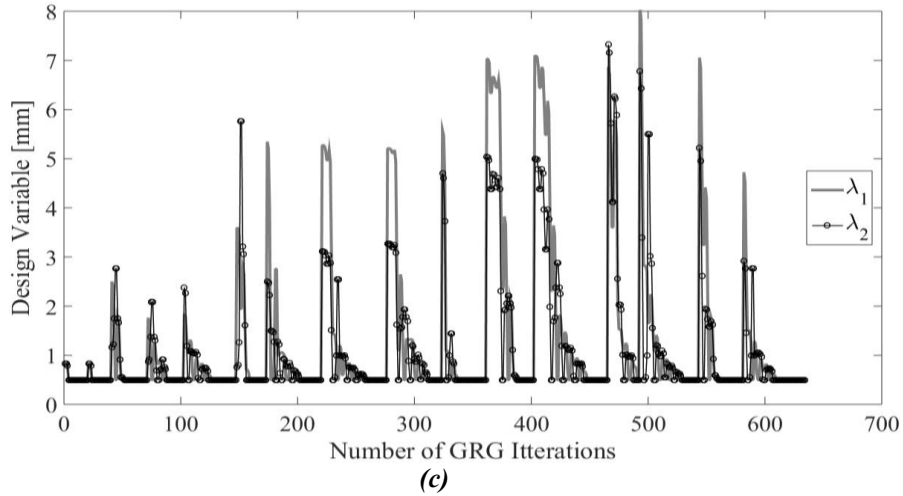


Figure 4.7: Optimization study SS-Slit-1 SARGSTEN convergence history of (a) the objective function in terms of the OASPL, (b) the slit design variable h , and (c) λ_1 and λ_2

The noise spectrums for both a straight TE and each of the optimized, single-size, slitted TE designs are given in Figure 4.8. Of the single-size slit optimization studies, the design that produced the least noise was SS-Slit-3, which produced an OASPL of 32.02 dB, a 10.38% reduction compared to the straight trailing edge. Similar to the single-size sawtooth optimization, SS-Slit-3 also applied the largest upper limit on the slit amplitude, h , and the smallest lower limits on widths, λ_1 and λ_2 . In all single-size slit studies, the optimum widths are seen to be equal to their lower limits of $(\lambda_1)_{\min}$ and $(\lambda_2)_{\min}$. Herr [54] found the same optimal condition for the slit and gap widths and attributed it to the thickness of the viscous sublayer. The optimum slit amplitude, h_{opt} ; however, is not equal to its upper limit, h_{max} , and instead has a specific value of 3.275 mm. Regardless of the bounds applied in the SS-Slit studies, no h_{opt} value was found to be similar to the best performing slitted TE designs studied in the literature [46, 54, 95]. In a study of TE noise reduction using TE brushes, Herr [54] found that the optimum brush length ranged between 30 mm and 60 mm. While the brush length values are of an order of magnitude larger than the h_{opt} values obtained in the SS-Slit studies, the optimum range that Herr gave for brush

length is far from the maximum length tested of 100 mm. This suggests that maximum noise reduction from non-oblique serrations (i.e., slits and brushes) is achieved with a finite, and particular, length that corresponds to enhancement of the physical, noise reduction, mechanisms.

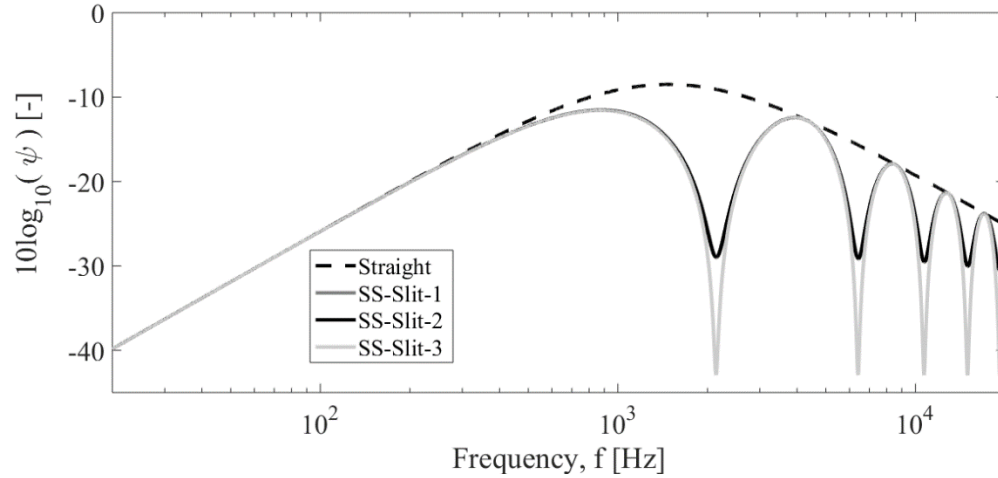


Figure 4.8: SPL plotted as a function of frequency between 20 Hz and 20 kHz for optimum single size slitted trailing edge profiles.

The influence of the slitted geometry parameters was investigated further. It was found that the slit and gap widths, λ_1 and λ_2 , respectively, control the value of the SPL at the peak reduction frequencies, $\psi(f_{\text{peak}}^n)$. The relation of λ_1 and λ_2 to $\psi(f_{\text{peak}}^n)$ is best described using two different width parameters: the total slitted serration width, λ_{1+2} , which is the sum of λ_1 and λ_2 , and the slit-to-gap width ratio, $\lambda_{1/2}$, which is the ratio of λ_1 to λ_2 . A reduction in λ_{1+2} results in a decrease of $\psi(f_{\text{peak}}^n)$ and, as $\lambda_{1/2}$ approaches 1, $\psi(f_{\text{peak}}^n)$ will again decrease. The dependence of noise reduction level on both λ_1 and λ_2 is in agreement with observations made in the literature [46, 47, 54, 95, 96]; however, no explicit discussion of the double dependence on λ_{1+2} and $\lambda_{1/2}$ was made. Further, it was also found that the value of $\psi(f_{\text{peak}}^n)$ is independent of h , which contradicts the result found by Gruber

et al. [46]. In Ref. [46], Gruber *et al.* found that the noise reduction level increases with decreasing values of λ_{1+2}/h , which suggests that $\psi(f_{\text{peak}}^n)$ is inversely proportional to h , and should increase with an increase in slit amplitude.

Similar to the single-size sawtooth TE, it was found that the h value of a single-size slitted TE controls the peak reduction frequencies, f_{peak}^n . In this case, however, the functional dependence of f_{peak}^n on h is the following:

$$(f_{\text{peak}}^n)_{\text{slit}} = \left(n - \frac{1}{2}\right) \left(\frac{U_c}{2h}\right) \text{ for } n = 1, 2, 3, \dots \quad (4.3)$$

It then follows, from Eqn. (4.3), that the first reduction peak, f_{peak}^1 , is given by the ratio $U_c/4h$, which decreases with increasing h , i.e., the first reduction peak occurs at a lower frequency, for a longer slit. By inspection of Figure 4.8 and Eqn. (4.3), it is seen that the peak-to-peak frequency bandwidth, Δf_{peak} , is now equal to $2f_{\text{peak}}^1$, but is still constant across the entire spectrum for a given h value. Equation (4.3) is in agreement with the relation given in Ref. [47] by Azarpeyvand *et al.* (in non-dimensional form) for, what they called, the “harmonic dips” in the slitted TE noise spectrums. While Gruber *et al.* [46] also found that f_{peak}^n is independent of the slit and gap widths, the slitted f_{peak}^n equation given there is not consistent with Eqn. (4.3), and does not match results presented in this thesis.

From inspection of Figure 4.8 and numerical investigation of design variable trends, four different factors have been identified that set the specific value of h_{opt} found in each SS-Slit study. The factors are as follows:

- (i) Maximum noise reduction occurs at f_{peak}^n (calculated using Eqn. (4.3));
- (ii) Larger noise reductions for frequencies near f_{peak}^n ;
- (iii) $\psi_{\text{slit}}(f_{\text{hump}}^1) < \psi_0(f_{\text{hump}}^1)$;

- (iv) As Δf_{peak} is decreased, the number of reduction peaks that occur within the range $(f_{\text{min}}, f_{\text{max}})$ increases.

While all four factors contribute to the value of h_{opt} , the relative importance of each factor is dependent on the value of $\psi(f_{\text{peak}}^1)$, and therefore also on the values of λ_1 and λ_2 . As $\psi(f_{\text{peak}}^1)$ is reduced (i.e., increase in peak noise reduction), (i) and (ii) influence the value of h_{opt} more heavily. This occurs because it becomes more beneficial for the noise reduction peak to be positioned at/near the extremum point in the straight TE spectrum.

4.3 Frequency Dependent Serrations

4.3.1 Sawtooth

The noise spectrum for both a straight TE and each of the optimized, frequency-dependent, sawtooth TE designs is given in Figure 4.9. Of the frequency-dependent sawtooth TE optimization studies, the optimal design from FD-Saw-1 produced the least noise with an OASPL of 9.022 dB. This sawtooth TE resulted in a 74.75% reduction in OASPL compared to the straight TE, as well as a 31.62% reduction compared to the best SS-Saw TE design (SS-Saw-5). The optimum sawtooth width was again equal to the lower limit used in the study; however, the optimum value for the sawtooth amplitude, h_{opt} , was not a constant value.

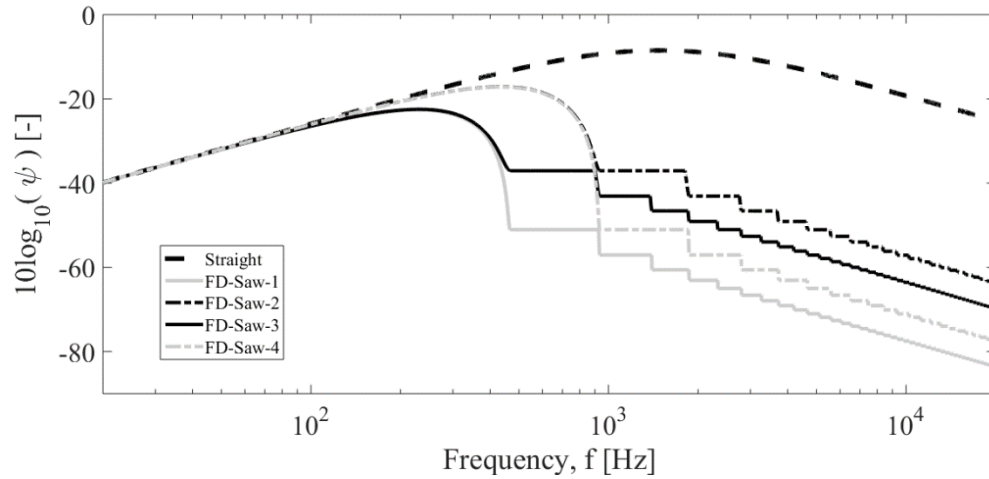


Figure 4.9: SPL plotted as a function of frequency between 20 Hz and 20 kHz for optimum frequency-dependent sawtooth trailing edge profiles.

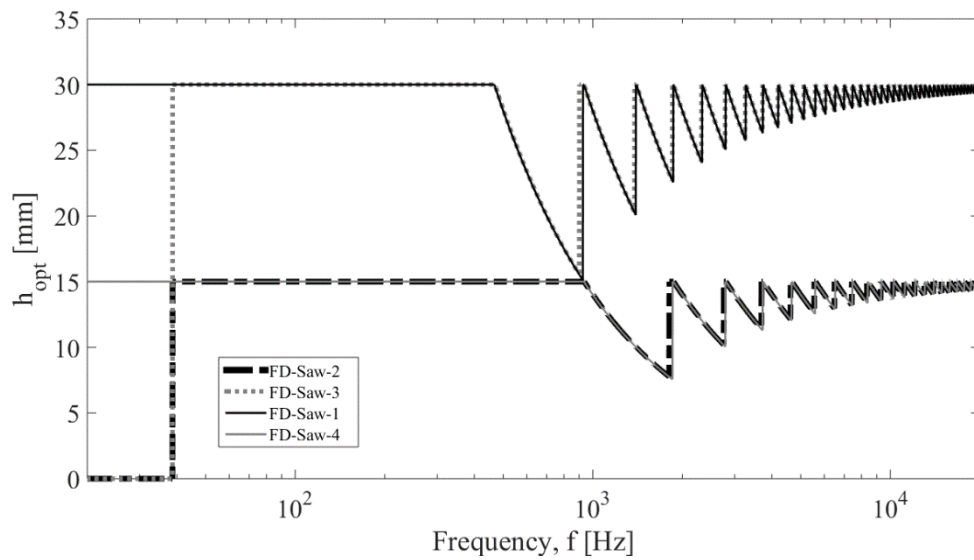


Figure 4.10: Optimum sawtooth amplitude plotted as a function of frequency between 20 Hz and 20 kHz for optimum frequency-dependent sawtooth trailing edge profiles.

The variation in h_{opt} across frequency is shown in Figure 4.10, where three distinct frequency ranges of interest can be seen for each design. The lower frequency range is defined as the frequency band where h_{opt} equals zero, i.e., where a straight TE produces less noise than a sawtooth TE of any size. This range includes frequencies between f_{min} , the lowest frequency of interest, and f_{reduc} , the frequency at which a sawtooth TE produces

less noise than a straight TE. It was found that f_{reduc} is a function of λ where a decrease in serration width reduces f_{reduc} . This means that for a sufficiently small λ , f_{reduc} will be lower than f_{min} , therefore, allowing noise reduction to occur via a sawtooth TE at all frequencies of interest. It can be seen in Figure 4.10 that FD-Saw-1 has a small enough width for this condition to be true. In the mid frequency range, the h_{opt} value suddenly jumps to its maximum value, and stays constant for the entire range. This range starts where the jump occurs, at f_{reduc} , and ends at the frequency f_{peak^1} , which is calculated from Eqn. (4.2). The high frequency range consists of all frequencies between f_{peak^1} and f_{max} , the highest frequency of interest. In this range, h_{opt} is an oscillatory function of frequency, which has a diminishing oscillation amplitude with increasing frequency as it converges towards h_{max} . In this range, the h_{opt} function corresponds to the reduction peaks, and it is obtained from rearranging Eqn. (4.2) to give serration amplitude as a function of frequency. This rearranged version of Eqn. (4.2) is given here for reference as follows:

$$h_{\text{opt}} = n \left(\frac{U_c}{2f} \right) \text{ for } n = 1, 2, 3, \dots \quad (4.4)$$

The function is smooth and continuous for each n -band, defined as $f_{\text{peak}^n} < f < f_{\text{peak}^{(n+1)}}$, but jumps back to h_{max} as the frequency is increased above each $f_{\text{peak}^{(n+1)}}$. The value of n in Eqn. (4.4) is constant in each n -band, and increases by one for each successively higher frequency n -band. The implication of the three frequency ranges, and smaller, high-frequency n -bands, is that it may be possible to design a multi-tooth-size sawtooth TE to target certain frequency ranges for increased noise reduction. Examples of such designs are shown in Figure 4.11 and Figure 4.12, which are referred to as the Saw–Saw serration and a Saw+Saw serration, respectively.

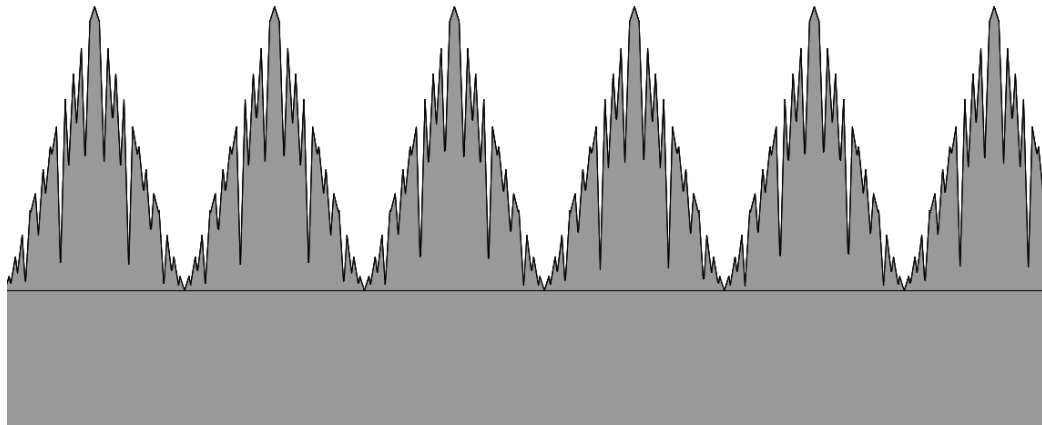


Figure 4.11: Example of a Saw-Saw trailing edge serration profile design.

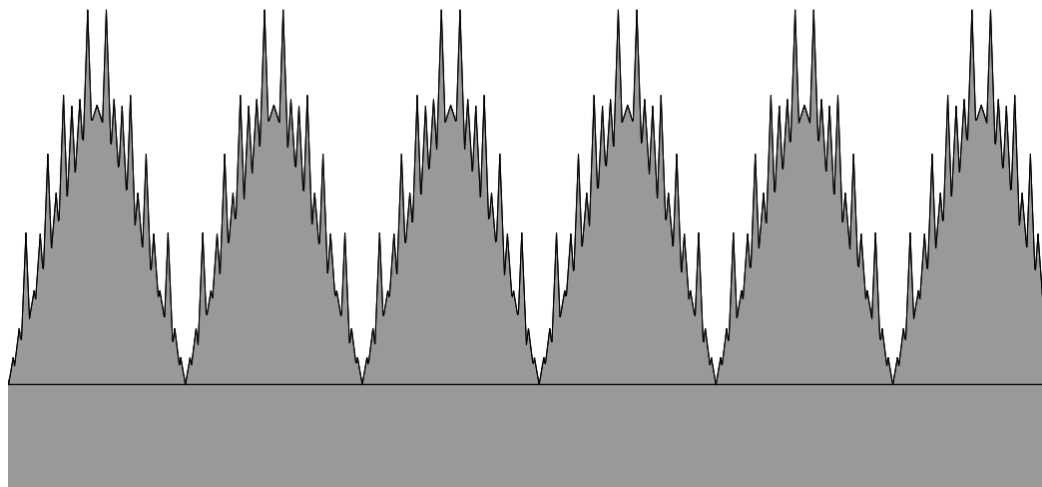


Figure 4.12: Example of a Saw+Saw trailing edge serration profile design.

The Saw—Saw design (Figure 4.11) has a large base sawtooth with inverted sawtooth shapes of various amplitudes cut out of the base profile. The inverted sawtooth cut-outs are distributed along the base sawtooth's edge, and both the base sawtooth and inverted sawtooth cut-outs are oriented in the streamwise direction. Superimposing sawtooth shapes allows the serrated TE to target a number of different turbulent structure sizes within one base sawtooth width in the spanwise direction.

Another version of a multi-tooth-size sawtooth TE can be created by distributing sawteeth of various sizes across the span of the TE. Gruber *et al.* [95] proposed and tested a spanwise distributed multi-tooth-size sawtooth TE to investigate its broadband noise reduction capabilities. Their design distributed a wide range of sawtooth sizes randomly along the span according to a normal distribution probability function. The Random sawtooth TE produced modest noise reductions (1 ~ 3 dB) in the low and mid frequency range; however, these reductions were less than both the single-size sawtooth and slitted trailing edges they tested. The lack of improvement over single-size TE serrations is likely due to the use of non-optimal sizes being introduced by the random distribution, as well as the inability to target multiple sizes of turbulent structures in the same spanwise location. Both of these deficiencies are addressed by the novel superimposed sawtooth designs given in Figure 4.11 and Figure 4.12.

4.3.2 Slitted

The noise spectrum for both a straight TE and each of the optimized, frequency-dependent, slitted TE designs is given in Figure 4.13. Compared to all other designs examined in this thesis, the FD-Slit-3 design, from the frequency-dependent slitted TE optimization studies, produced the minimum amount of noise, with an OASPL of 8.855 dB. FD-Slit-3 gives a 75.31 % reduction in OASPL compared to the straight TE, a 72.33 % reduction compared to the least-noise single-size slit design (SS-Slit-3), and a 1.85% reduction compared to the least-noise frequency-dependent sawtooth design (FD-Saw-1). This result does not follow the same pattern as the single-size serration designs, where all of the sawtooth serrations significantly outperformed the slitted serrations. This suggests that slit style TE serrations may actually be just as, if not more, effective than sawtooth TE

serrations at reducing TBL-TE noise if applied in an appropriate way, i.e., as a distribution of multiple sizes instead of a single-size slitted TE. This finding contradicts Gruber *et al.* [46], where it is stated that slit serrations are not an effective noise reduction treatment.

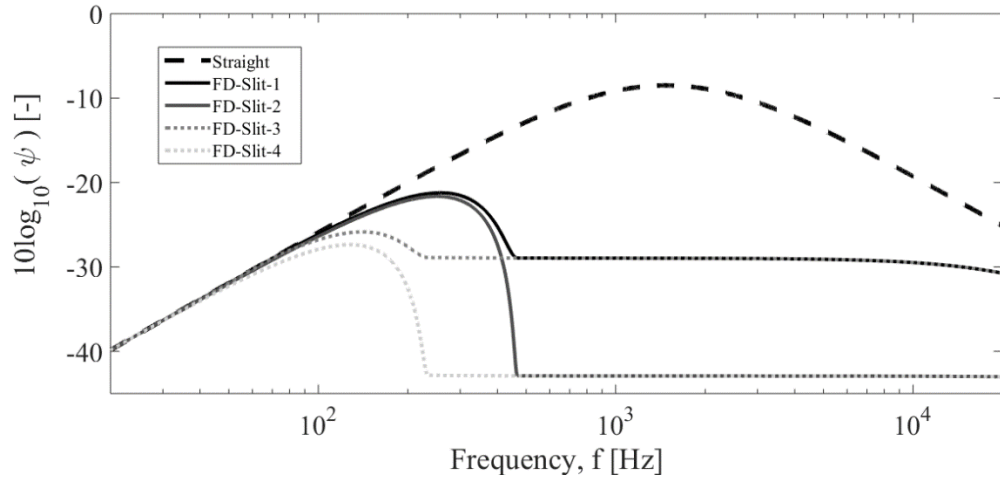


Figure 4.13: SPL plotted as a function of frequency between 20 Hz and 20 kHz for optimum frequency-dependent slitted trailing edge profiles.

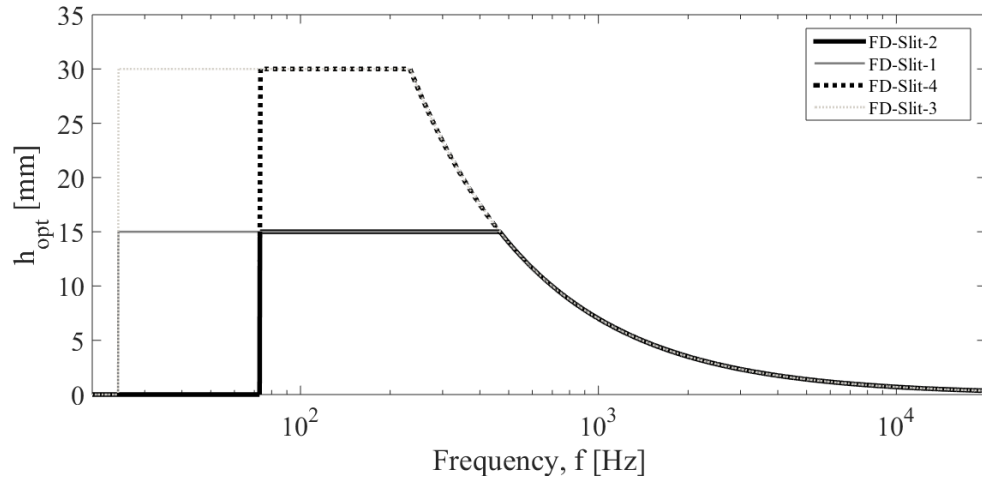


Figure 4.14: Optimum slit amplitude plotted as a function of frequency between 20 Hz and 20 kHz for optimum frequency-dependent slitted trailing edge profiles.

The optimal FD-Slit-3 design has constant values of $(\lambda_1)_{opt}$ and $(\lambda_2)_{opt}$, equal, first to each other, and then to the larger of $(\lambda_1)_{min}$ and $(\lambda_2)_{min}$ for all frequencies. The variations in h_{opt} across frequency are shown in Figure 4.14 for the optimized frequency-dependent

slitted TE designs. From inspection of this figure, it is shown that the value of h_{opt} is dependent on frequency, and there are three important frequency ranges that define h_{opt} . These frequency ranges are similar, but not equal, to the low, mid, and high ranges in the frequency-dependent sawtooth TE optimization studies. In the low frequency range, h_{opt} is equal to zero, meaning that a straight TE produces less noise at these low frequencies than any feasible slit serration. This low frequency range has a lower bound of f_{min} , and an upper bound of f_{reduc} . For the frequency-dependent slitted TE it was found that f_{reduc} is dependent on both λ_1 and λ_2 . In order to reduce f_{reduc} , the total serration width, λ_{1+2} , must be reduced, and the slit-to-gap width ratio, $\lambda_{1/2}$, must be increased. In the mid frequency range, defined as all frequencies between f_{reduc} and f_{peak}^1 , h_{opt} is constant, and is equal to its maximum value, h_{max} . The upper bound on this mid frequency range, f_{peak}^1 , is calculated using Eqn. (4.3) with $n = 1$. In the high frequency range, which has a lower bound of f_{peak}^1 , and upper bound of f_{max} , h_{opt} is a smooth and continuous function of frequency. The value of h_{opt} , at any frequency in this range, is calculated using a rearranged version of Eqn. (4.3) (with $n = 1$) to give h_{opt} as a function of frequency. The resulting h_{opt} function is the following:

$$h_{\text{opt}} = \left(\frac{U_c}{4f} \right) \text{ for } f > f_{\text{peak}}^1 \quad (4.5)$$

Unlike the frequency-dependent sawtooth TE designs, there are no n-band oscillations in the value of h_{opt} at high frequencies observed in Figure 4.14. A multi-tooth-size slitted TE could also be designed to target specific frequency ranges for TBL-TE noise reduction. In this case; however, the frequency range(s) targeted may experience maximum reductions while noise from other, non-targeted, frequencies may not be reduced at all, or the reduction would be much less. This is because there are no high frequency h_{opt}

oscillations; therefore, each frequency has a unique optimum slit amplitude, which is not optimal for any other frequency.

Chapter 5

CONCLUSIONS

5.1 Summary and Contributions to the State of the Art

The reduction of TBL-TE noise using flat-plate type TE serrations predicted by semi-empirical models was examined through optimization studies. Two different serration shapes were investigated, in both broadband and narrow band optimization studies. The optimization studies were carried out using the optimization code, SAGRGSTEN, developed in-house, by the author for this thesis.

Throughout the work included in this thesis, a number of unique and novel contributions have been made to the state of the art as follows:

- (i) The numerical optimization program, SAGRGSTEN, was developed. The program is based on both the SA algorithm and the GRG algorithm. The use of the SA algorithm for selecting starting points to be sent to the GRG algorithm is a novel construction of a hybrid optimization algorithm. The entirety of the code was written in-house by the author using the MATLAB language. A description of the code is given in Chapter 3.

- (ii) A thorough verification and validation of the optimization program SAGRSTEN, and its components was conducted. The implementation of the SA and GRG algorithms, as well as the combination of the two (as a new hybrid method) was rigorously verified to ensure correct functionality in all applicable conditions. Additionally, a discussion regarding the validity of Howe's semi-empirical TBL-TE noise model for a serrated TE was presented. By direct comparison to published experimental results, it was established that Howe's model is an appropriate noise prediction tool for the work in this thesis.
- (iii) A framework for the numerical optimization of noise reducing TE serrations was developed. The framework includes a novel approach to optimizing for TBL-TE noise reduction, which uses semi-empirical noise models to calculate the objective function values. Previous efforts towards TBL-TE noise reduction optimization were limited to experimental trial and error of a finite number of geometry variations and elaborate numerical simulations employing CAA, both of which are time consuming and costly. The optimization framework established in this thesis provides a means of conducting highly efficient TBL-TE noise optimization studies.
- (iv) Four different types of optimization studies were conducted, regarding the reduction of TBL-TE noise using TE serrations. These consisted of two different serration geometries, sawtooth and slitted, which were each optimized for both broadband (20 Hz to 20 kHz) as well as all individual frequencies (between 20 Hz and 20 kHz). Theoretical conditions of optimality for the serrations were established and compared to the literature.

- (v) Sensitivity of the TBL-TE noise spectrum to changes in TE serration parameters was investigated. Based on the behavior and response of the spectrums, two new serration profiles (Saw–Saw and Saw+Saw) were proposed. These two profiles can be specifically tailored to target desired frequency ranges. The concept of superimposing multiple sawtooth sizes is a variation of previously studied profiles like the Slitted-Sawtooth and Random TE serrations.

5.2 Conclusions

The single-size sawtooth optimization studies showed that the best performing sawtooth TE (in terms of noise reduction) found experimentally is, in fact, the optimum geometry. This is, however, only the case when the design variable limits are set based on the manufacturing limits given by Gruber *et al.* [46]. It then follows that in order to achieve greater noise reductions with a single-size sawtooth TE, the manufacturing limits must be loosened.

It was shown in optimization studies SS-Saw-3 to SS-Saw-5 that loosening the design variable limits, beyond manufacturing limits, can potentially lead to significant improvements in noise reduction. Further, since the manufacturing limit on λ_{\min} is much tighter than the one on h_{\max} , greater improvements can be obtained by focusing on extending the sawtooth root-to-tip length.

From further investigation of the single-size sawtooth parameter sensitivity, possible conditions for optimality were defined. It was found that the single-size sawtooth TE that produces the overall least noise always has the largest feasible amplitude and smallest feasible width. That is to say that, $h_{\text{opt}} = h_{\max}$, and $\lambda_{\text{opt}} = \lambda_{\min}$.

The single-size slit optimization studies did not give optimum geometries that are consistent with any tested experimentally so far. The specific optimum design variable values have not yet, however, been examined experimentally.

The optimum single-size slitted serration was found to have the optimality condition that $\lambda_1 = \lambda_2$ first, and then that they have their smallest feasible slit and gap widths. This finding is in agreement with Azarpeyvand *et al.*'s [47] claim that $\lambda_1 = \lambda_2$ is a necessary condition to achieve maximum noise reduction. The optimum single-size slit amplitude was found to have a very specific value, and be independent of the design variable bounds on amplitude (for a sufficiently large design space). Further investigation into the slitted design variable sensitivity revealed that four factors, given in Section 4.2.2, contribute to the optimum amplitude value. It was also shown that the relative importance of each factor is dependent on the values of λ_1 and λ_2 , via the SPL at the first peak reduction frequency, $\Psi(f_{\text{peak}}^1)$.

Comparison of SS-Saw studies to SS-Slit showed that, while both geometries reduced noise from a straight TE, single-size sawtooth serrations give substantially more noise reduction than single-size slit serrations.

The frequency-dependent sawtooth optimization studies provided greater insight into the relation between sawtooth geometry and noise produced at each frequency. It was found that the condition $h_{\text{opt}} = h_{\text{max}}$, which was defined for a single-size sawtooth TE, does not apply to all frequencies in the spectrum. Three distinct frequency ranges that define the behavior of h_{opt} as a function of frequency were observed. It was found that, if the sawtooth serration width was not sufficiently small, a straight TE is optimum at lower frequencies. For the mid-frequency range, defined as $f_{\text{reduc}} < f < f_{\text{peak}}^n$, the condition $h_{\text{opt}} = h_{\text{max}}$ was

observed to be true and constant within this range. At higher frequencies ($f > f_{\text{peak}}^n$), however, sawtooth amplitude was seen to be a strong, oscillating function of frequency.

The total noise that would be produced by a sawtooth TE, with every frequency-optimized amplitude superimposed into a single tooth, was examined. It was found that substantially more noise reduction could be achieved by optimization at every frequency, instead of using the ‘best-fit’ approach as in the SS-Saw studies.

The frequency-dependent slitted TE optimization studies showed similar levels of frequency dependence to the FD-Saw studies. The optimum slit amplitude was found to be highly frequency dependent. Three frequency ranges, similar to the FD-Saw ranges, which define the optimum slit amplitude, were identified. The n-band oscillations, which were observed in the FD-Saw h_{opt} distribution, were not seen in the FD-Slit high frequency range. The FD-Slit h_{opt} distribution asymptotically decays from h_{max} towards zero; therefore, a unique slitted h_{opt} value exists for all $f > f_{\text{peak}}^n$.

Examination of the total noise that would be produced by a slitted TE, with every frequency-optimized amplitude superimposed into a single tooth, revealed large noise reductions. It was seen that a serrated TE designed in this way could out-perform all SS-Slit, SS-Saw, and even FD-Saw designs in terms of noise reduction. It was thus determined that FD-Slit-3 gave the greatest amount of noise reduction, compared to all other optimum designs studied in this thesis.

5.3 Future Work

The serrated trailing edge optimization framework for noise reduction, and the studies produced from it in this thesis have contributed to advancements in TBL-TE noise

reduction research. Additionally, the work included in this thesis has also highlighted a number of new intriguing avenues that can be explored in future work. Potential extensions of this work follow two paths: (1) Numerical Analysis and Optimization, and (2) Experimental Studies. Specific examples of extension topics for each path are outlined below.

5.3.1 Extensions on the Numerical Analysis and Optimization

- (i) Sensitivity studies of the method used to predict serrated trailing edge noise in the SAGRSTEN program. Lyu *et al* [48] recently published a new, Amiet-based, analytical model for serrated TE noise prediction. This new model is claimed to be more consistent with experimental observations in literature, and give a more realistic prediction of noise reduction than Howe's model. Additionally, various CAA based methods can be used to predict the serrated TBL-TE noise. These methods would be significantly more computationally expensive than either Howe's or Lyu's model; however, they may also be more accurate.
- (ii) Optimization studies for additional serration geometries. Other serration geometries have been studied in the literature [47, 95] including sinusoidal, and random distribution, as well as super imposed shapes such as Saw-Sin, and Slit-Saw. Additionally, the novel serration profiles proposed in this thesis, Saw–Saw and Saw+Saw, can be optimized in terms of parameters defining the distribution of superimposed sawteeth.
- (iii) Optimization studies for other methods of TBL-TE noise reduction, and potentially combinations of methods. Graham's three owl wing attributes (see

Section 1.2.3) correspond to at least three different methods of TBL-TE noise reduction. It is therefore likely, from a bio-mimetic perspective, that the final, optimized solution is also a combination of methods.

- (iv) Multi-objective optimization studies that consider additional factors to noise reduction. As outlined in Chapter 1, in order to ensure industry acceptance of this technology, other, non-acoustic, factors must be considered. The general considerations made here can be quantified and modeled in terms of engineering specifications, and can then be converted into objective functions. Examples include flight performance, manufacturing costs/feasibility, maintenance costs, etc.
- (v) Sensitivity studies of variations to the definition of noise in the objective function. Since the need for noise reduction is driven by the perception of noise regularly experienced by humans, other methods of quantifying this effect may be appropriate. Of particular interest, are both the A-Weighted dB scale, dBA, and the Effective Perceived Noise Level, EPNdB. The dBA scale is important as ICAO noise standards are published in this scale, and EPNdB is important as it takes into consideration additional factors, such as the frequency spectrum shape and exposure duration [97].

5.3.2 Extensions into Experimental Studies

- (i) Investigate noise reduction abilities of the theoretical optimum geometries found in this thesis in experimental wind tunnel studies. Since all of the optimum designs were established based on a semi-empirical model, experimental results would allow comparison with in-house test data. This would allow for the

identification of additional factors that are possibly not captured in the model. Specifically, the optimum designs from the SS-Slit studies could be tested, as there are no published experimental results for the specific values of h_{opt} found.

- (ii) Experimental investigation of the conditions for optimality, and design variable trends proposed in this thesis. In addition to testing the specific designs, a series of wind tunnel experiments could be conducted to study, for example, whether or not the SS-Saw condition ($h_{opt} = h_{max}$ and $\lambda_{opt} = \lambda_{min}$) is always true.
- (iii) Experimental study of the TBL-TE noise produced by the novel Saw–Saw and Saw+Saw designs, proposed in this thesis. Wind tunnel measurements would not only establish the noise reduction ability of the designs, but could also advance the understanding of the mechanism(s) through which TE serrations reduce TBL-TE noise.

REFERENCES

- [1] Federal Aviation Administration, "Noise Standards: Aircraft Type and Airworthiness Certification," U.S. Department of Transportation, Washington DC, 2003.
- [2] S. Fidell, "Assessment of the effectiveness of aircraft noise regulation," *Noise and Health*, vol. 1, no. 3, pp. 17-26, 1999.
- [3] M. Kaltenbach, C. Maschke and R. Klinke, "Health Consequences of Aircraft Noise," *Deutsches Ärzteblatt International*, vol. 105, no. 32, p. 5488556, 2008.
- [4] L. Jarup, W. Babisch, D. Houthuijs, G. Pershagen, K. Katsouyanni, E. Cadum, M. Dudley, P. Savigny, I. Seiffert, W. Swart, O. Breugelmans, G. Bluhm, J. Selander, A. Haralabidis, K. Dimakopoulou, P. Sourtzi, M. Velonakis and F. VignaTaglianti, "Hypertension and exposure to noise near airports: The HYENA study," *Environmental Health Perspectives*, vol. 116, no. 3, pp. 329-333, 2008.
- [5] A. L. Hansell, M. Blangiardo, L. Fortunato, S. Floud, K. de Hoogh, D. Fecht, R. E. Ghosh, H. E. Laszlo, C. Pearson, L. Beale, S. Beevers, J. Gulliver, N. Best, S. Richardson and P. Elliott, "Aircraft noise and cardiovascular disease near

- Heathrow airport in London: small area study," *British Medical Journal*, vol. 347:f5432, 2013.
- [6] A. Correira, J. Peters, J. Levy, S. Melly and F. Dominici, "Residential exposure to aircraft noise and hospital admissions for cardiovascular diseases: Multiairport retrospective study," *British Medical Journal*, vol. 347, 2013.
- [7] ATAG, "Aviation Benefits Beyond Borders," ATAG, Geneva, 2014.
- [8] ICAO, "Air Navigation Report," ICAO, Montreal, 2015.
- [9] R. D. J. Shaufele, "Federal Aviation Administration Aerospace Forecast: Fiscal Years 2016-2036," Federal Aviation Administration, Wa, 2016.
- [10] R. Girvin, "Aircraft noise-abatement and mitigation strategies," *Journal of Air Transport Management*, vol. 15, no. 1, pp. 14-22, 2009.
- [11] D. Casalino, F. Diozzi, R. Sannino and A. Paonessa, "Aircraft noise reduction technologies: A bibliographic review," *Aerospace Science and Technology*, vol. 12, pp. 1-17, 2008.
- [12] W. Dobrzynski, "Almost 40 Years of Airframe Noise Research: What Did We Achieve?," *Journal of Aircraft*, vol. 47, no. 2, pp. 353-367, 2010.
- [13] A. Filippone, *Advanced Aircraft Flight Performance*, New York: Cambridge University Press, 2012.
- [14] R. Blockley, R. Agarwal, F. Collier, A. Schaefer and A. Seabridge, *Green Aviation*, Chichester: John Wiley & Sons Ltd, 2016.
- [15] T. F. Brooks, D. S. Pope and M. A. Marcolini, "Airfoil Self-Noise and Prediction," *NASA Reference Publication No. 1218*, 1989.

- [16] S. Wagner, R. Bareiss and G. Guidati, *Wind Turbine Noise*, Berlin: Springer-Verlag, 1996.
- [17] L. A. Errasquin, "Airfoil Self-Noise Prediction Using Neural Networks for Wind Turbines," Virginia Polytechnic Institute and State University, Blacksburg, 2009.
- [18] P. A. Davidson, *Turbulence: An Introduction for Scientists and Engineers*, New York: Oxford University Press, 2004.
- [19] M. S. Howe, *Acoustics of Fluid-Structure Interactions*, Cambridge: Cambridge University Press, 2008.
- [20] T. F. Brooks and T. H. Hodgson, "Trailing Edge Noise Prediction from Measured Surface Pressures," *Journal of Sound and Vibration*, vol. 78, no. 1, pp. 69-117, 1981.
- [21] T. Dassen, R. Parchen, G. Guidati, S. Wagner, S. Kang and A. E. Khodak, "Comparison of measured and predicted airfoil self-noise with application to wind turbine noise reduction," NLR, Amsterdam, 1997.
- [22] M. Roger and S. Moreau, "Extensions and limitations of analytical airfoil broadband noise models," *International Journal of Aeroacoustics*, vol. 9, no. 3, pp. 273-305, 2010.
- [23] D. J. Moreau, L. A. Brooks and C. J. Doolan, "Experimental investigation of broadband trailing edge noise from sharp-edged struts," in *17th AIAA/CEAS Aeroacoustics Conference*, Portland, 2011.

- [24] M. Kamruzzaman, T. Lutz, W. Würz, W. Z. Shen, W. J. Zhu, M. O. L. Hansen, F. Bertagnolio and H. A. Madsen, "Validations and improvements of airfoil trailing-edge noise prediction models using detailed experimental data," *Wind Energy*, vol. 15, no. 1, pp. 45-61, 2012.
- [25] M. Tuinstra, S. Pröbsting and F. Scarano, "On the use of Particle Image Velocimetry to predict trailing edge noise," in *19th AIAA/CEAS Aeroacoustic Conference*, Berlin, 2013.
- [26] R. D. Sandberg and L. E. Jones, "Direct Numerical Simulations of Airfoil Self-Noise," in *IUTAM Symposium on Computational Aero-Acoustics for Aircraft Noise Prediction*, Southampton, 2010.
- [27] S. Hosder, J. A. Schetz, W. H. Mason, B. Grossman and R. T. Haftka, "Computational-Fluid-Dynamics-Based Clean-Wing Aerodynamic Noise Model for Design," *Journal of Aircraft*, vol. 47, no. 3, pp. 754-762, 2010.
- [28] T. Do, L. Chen and J. Tu, "Numerical study of turbulent trailing-edge flows with base cavity effects using URANS," *Journal of Fluids and Structures*, vol. 26, no. 1, pp. 1155-1173, 2010.
- [29] M. Jiang, X. Li, B. Bai and D. Lin, "Numerical simulation on the NACA0018 airfoil self-noise generation," *Theoretical and Applied Mechanics Letters*, vol. 2, no. 1, pp. 052004-1-4, 2012.
- [30] R. Arina, D. R. R. Rinaldi and A. Iob, "Numerical Study of Self-Noise Produced by an Airfoil with Trailing-Edge Serrations," in *18th AIAA/CEAS Aeroacoustics Conference*, Colorado Springs, 2012.

- [31] J. E. Ffowcs Williams and L. H. Hall, "Aerodynamic Sound Generation by Turbulent Flow in the Vicinity of a Scattering Half Plane," *Journal of Fluid Mechanics*, vol. 40, no. 4, pp. 657-670, 1970.
- [32] D. M. Chase, "Sound radiated by turbulent flow off a rigid half-plane as obtained from a wavenumber spectrum of hydrodynamic pressure," *Journal of the Acoustical Society of America*, vol. 52, no. 1, pp. 1011-1023, 1972.
- [33] K. L. Chandiramani, "Diffraction of evanescent waves, with applications to aerodynamically scattered sound and radiation from un baffled plates," *Journal of the Acoustical Society of America*, vol. 55, pp. 19-29, 1974.
- [34] D. M. Chase, "Noise radiated from an edge in turbulent flow," *American Institute of Aeronautics and Astronautics Journal*, vol. 13, pp. 1041-1047, 1975.
- [35] R. K. Amiet, "Acoustic Radiation From an Airfoil in a Turbulent Stream," *Journal of Sound and Vibration*, vol. 41, no. 4, pp. 407-420, 1975.
- [36] R. K. Amiet, "Noise Due to Turbulent Flow Past a Trailing Edge," *Journal of Sound and Vibration*, vol. 47, no. 3, pp. 387-393, 1976.
- [37] R. K. Amiet, "Effect of the incident surface pressure field on noise due to turbulent flow past a trailing edge," *Journal of Sound and Vibration*, vol. 57, no. 2, pp. 305-306, 1978.
- [38] M. S. Howe, "A Review of the Theory of Trailing Edge Noise," *Journal of Sound and Vibration*, vol. 61, no. 3, pp. 437-465, 1978.

- [39] M. Roger and S. Moreau, "Back-scattering correction and further extensions of Amiet's trailing-edge noise model. Part 1: theory," *Journal of Sound and Vibration*, vol. 286, no. 1, pp. 477-506, 2005.
- [40] S. Moreau and M. Roger, "Back-scattering correction and further extensions of Amiet's trailing-edge noise model. Part 2: Application," *Journal of Sound and Vibration*, vol. 323, no. 1, pp. 397-425, 2009.
- [41] A. Powell, "On the Aerodynamic Noise of a Rigid Flat Plate Moving at Zero Incidence," *The Journal of the Acoustical Society of America*, vol. 31, no. 12, pp. 1649-1653, 1959.
- [42] S. M. Kuo and D. R. Morgan, "Active Noise Control: A Tutorial Review," *Proceedings of the IEEE*, vol. 87, no. 6, pp. 943-973, 06 August 1999.
- [43] M. Fink and D. Bailey, "Model tests of airframe noise reduction concepts," in *6th Aeroacoustics Conference*, Hartford, 1980.
- [44] M. S. Howe, "Aerodynamic Noise of a Serrated Trailing Edge," *Journal of Fluids and Structures*, vol. 5, pp. 33-45, 1991.
- [45] M. S. Howe, "Noise produced by a sawtooth trailing edge," *Journal of the Acoustical Society of America*, vol. 90, no. 1, pp. 482-487, 1991.
- [46] M. Gruber, M. Azarpeyvand and P. F. Joseph, "Airfoil trailing edge noise reduction by the introduction of sawtooth and slitted trailing edge geometries," in *20th International Congress on Acoustics*, Sydney, 2010.

- [47] M. Azarpeyvand, M. Gruber and P. F. Joseph, "An analytical investigation of trailing edge noise reduction using novel serrations," in *19th AIAA/CEAS Aeroacoustics Conference*, Berlin, 2013.
- [48] B. Lyu, M. Azarpeyvand and S. Sinayoko, "Prediction of noise from serrated trailing edges," *Journal of Fluid Mechanics*, vol. 793, no. 1, pp. 556-588, 18 March 2016.
- [49] T. Bachmann, S. Klän, W. Baumgartner, M. Klaas, W. Schröder and H. Wagner, "Morphometric characterisation of wing feathers of the barn owl," *Frontiers in Zoology*, vol. 4, no. 1, pp. 23-38, 2007.
- [50] G. M. Lilley, "A Study of the Silent Flight of the Owl," in *4th AIAA/CEAS Aeroacoustics Conference*, Toulouse, 1998.
- [51] R. R. Graham, "The silent flight of owls," *Royal Aeronautical Society Journal*, vol. 286, pp. 837-843, 1934.
- [52] R. A. Kroeger, H. D. Gruschka and T. C. Helvey, "Low Speed Aerodynamics for Ultra-Quiet Flight," Air Force Flight Dynamics Laboratory, Tullahoma, 1971.
- [53] T. Bachmann and H. Wagner, "Silent Owl Wings," in *Encyclopedia of Nanotechnology*, Dordrecht, Springer Netherlands, 2012, pp. 2411-2420.
- [54] M. Herr, "Design Criteria for Low-Noise Trailing-Edges," in *13th AIAA/CEAS Aeroacoustics Conference*, Rome, 2007.
- [55] T. Bachmann, H. Wagner and C. Tropea, "Inner vane fringes of barn owl feathers reconsidered: morphometric data and functional aspects," *Journal of Anatomy*, vol. 221, no. 1, pp. 1-8, 2012.

- [56] "Design and testing of acoustically optimized airfoils for wind turbines," Non-Nuclear Energy Program, Contract JOR3-CT98-0248, 1998.
- [57] G. Guidati and S. Wagner, "Design of Reduced Noise Airfoils for Wind Turbines," in *European Congress on Computational Methods in Applied Sciences and Engineering*, Barcelona, 2000.
- [58] P. Fuglsang and H. A. Madsen, "Optimization method for wind turbine rotors," *Journal of Wind Engineering and Industrial Aerodynamics*, vol. 80, pp. 191-206, 1999.
- [59] A. L. Marsden, M. Wang and B. Mohammadi, "Shape optimization for aerodynamic noise control," Stanford University: Center for Turbulence Research, Stanford, 2001.
- [60] A. L. Marsden, M. Wang and P. Koumoutsakos, "Optimal aeroacoustic shape design using approximation modeling," Stanford University: Center for Turbulence Research, Stanford, 2002.
- [61] A. L. Marsden, M. Wang, J. E. Dennis, Jr. and P. Moin, "Optimal Aeroacoustic Shape Design Using the Surrogate Management Framework," *Optimization and Engineering*, vol. 5, pp. 235-262, 2004.
- [62] A. L. Marsden, M. Wang, J. J. E. Dennis and P. Moin, "Trailing-edge noise reduction using derivative-free optimization and large-eddy simulation," *Journal of Fluid Mechanics*, vol. 572, pp. 13-36, 2007.

- [63] T. Lutz, W. Würz, A. Herrig, K. Braun and S. Wagner, "Numerical Optimization of Silent Airfoil Sections," in *DEWEK 2004, 7th German wind energy conference*, Wilhelmshaven, 2004.
- [64] M. S. Howe, "Contributions to the theory of aerodynamic sound, with application to excess jet noise and the theory of the flute," *Journal of Fluid Mechanics*, vol. 71, no. 4, pp. 625-673, 1975.
- [65] D. G. Crighton and F. G. Leppington, "Scattering of aerodynamic noise by a semi-infinite compliant plate," *Journal of Fluid Mechanics*, vol. 43, pp. 721-736, 1970.
- [66] M. S. Howe, "Edge-source acoustic Green's function for an airfoil of arbitrary chord, with application to trailing-edge noise," *The Quarterly Journal of Mechanics and Applied Mathematics*, vol. 54, pp. 139-155, 2001.
- [67] D. M. Chase, "The Character of the Turbulent Wall Pressure Spectrum at Subconvective Wavenumbers and a Suggested Comprehensive Model," *Journal of Sound and Vibration*, vol. 112, no. 1, pp. 125-147, 1987.
- [68] R. F. Jones, C. J. Doolan and M. D. Teubner, "Minimization of trailing edge noise by parametric airfoil shape modifications," in *17th AIAA/CEAS Aeroacoustics Conference*, Portland, 2011.
- [69] F. Bertagnolio, H. A. Madsen and C. Bak, "Trailing Edge Noise Model Validation and Application to Airfoil Optimization," *Journal of Solar Energy Engineering*, vol. 132, pp. 1-9, 2010.
- [70] F. M. White, *Viscous Fluid Flow*, 3rd ed., New York: McGraw-Hill, 2014.

- [71] M. Drela and H. Youngren, "XFOIL: Subsonic Airfoil Development System," MIT, December 2013. [Online]. Available: <http://web.mit.edu/drela/Public/web/xfoil/>. [Accessed July 2016].
- [72] T. Göçmen and B. Özerdem, "Airfoil optimization for noise emission problem and aerodynamic performance criterion on small scale wind turbines," *Energy*, vol. 46, pp. 62-71, 2012.
- [73] M. Gruber, "Airfoil noise reduction by edge treatments, PhD thesis," University of Southampton, Southampton, 2012.
- [74] T. P. Chong and A. Vathylakis, "On the aeroacoustic and flow structures developed on a flat plate with a serrated sawtooth trailing edge," *Journal of Sound and Vibration*, vol. 354, pp. 65-90, 2015.
- [75] J. W. Chinneck, *Practical Optimization: A Gentle Introduction*, Ottawa, 2015.
- [76] S. S. Rao, *Engineering Optimization: Theory and Practice*, 4th ed., Hoboken: John Wiley & Sons Inc., 2009.
- [77] A. R. Parkinson, R. J. Balling and J. D. Hedengren, *Optimization Methods for Engineering Design*, Provo: Brigham Young University, 2013.
- [78] R. K. Arora, *Optimization: Algorithms and Applications*, Boca Raton: Taylor & Francis Group, LLC, 2015.
- [79] U. Diwekar, *Introduction to Applied Optimization*, 3rd ed., New York: Springer Science+Business Media, LLC, 2008.
- [80] T. F. Edgar, D. M. Himmelblau and L. S. Lasdon, *Optimization of Chemical Processes*, New York: McGraw Hill, 2001.

- [81] J. Nocedal and S. J. Wright, Numerical Optimization, New York: Springer-Verlag New York, Inc., 1999.
- [82] E. Sandgren and K. M. Ragsdell, "The utility of nonlinear programming algorithms: A comparative study, Parts 1 and 2," *ASME Journal of Mechanical Design*, vol. 102, no. 3, pp. 540-551, 1980.
- [83] K. Schittkowski, "Nonlinear Programming codes: Information, Tests, Performance," in *Lecture Notes in Economics and Mathematical Systems*, vol. 183, New York, Springer-Verlag, 1980, p. Vol. 183.
- [84] V. Plevris and M. Papadrakakis, "A Hybrid Particle Swarm-Gradient Algorithm for Global Structural Optimization," *Computer-Aided Civil and Infrastructure Engineering*, vol. 26, pp. 48-68, 2011.
- [85] J. Liu, S. Zhang, C. Wu, J. Liang, X. Wang and K. Teo, "A hybrid approach to constrained global optimization," *Applied Soft Computing*, vol. 47, no. 1, pp. 281-294, 2016.
- [86] K. Miettinen, M. Mäkelä and H. Maaranen, "Efficient hybrid methods for global continuous optimization based on simulated annealing," *Computers & Operations Research*, vol. 33, no. 1, pp. 1102-1116, 2006.
- [87] P. J. M. van Laarhoven and E. H. Aarts, Simulated Annealing: Theory and Applications, vol. 37, Eindhoven: Springer Netherlands, 1987.
- [88] L. S. Lasdon, R. Fox and M. Ratner, "Nonlinear optimization using the generalized reduced gradient method," Dept. of Oper. Res., Case Western Reserve University, Cleveland, 1973.

- [89] L. S. Lasdon, A. D. Waren, A. Jain and M. Ratner, "Design and testing of a generalized reduced gradient code for nonlinear programming," *ACM Transactions on Mathematical Software*, vol. 4, no. 1, pp. 34-50, 1978.
- [90] K. A. Kopecky, "Computational Methods for Macroeconomics: Numerical Differentiation Lecture Notes," The University of Western Ontario, London, 2007.
- [91] D. G. Zill, W. S. Wright and M. R. Cullen, *Advanced Engineering Mathematics*, 4th ed., Sudbury: Jones and Bartlett Publishers LLC, 2011.
- [92] D. J. Moreau and C. J. Doolan, "Noise-Reduction Mechanism of a Flat-Plate Serrated Trailing Edge," *AIAA Journal*, vol. 51, no. 10, pp. 2513-2522, 2013.
- [93] M. Gruber, P. Joseph and T. P. Chong, "On the mechanisms of serrated airfoil trailing edge noise reduction," in *17th AIAA/CEAS Aeroacoustics Conference*, Portland, 2011.
- [94] S. Oerlemans, M. Fisher, T. Maeder and K. Kögler, "Reduction of Wind Turbine Noise Using Optimized Airfoils and Trailing-Edge Serrations," *AIAA Journal*, vol. 47, no. 6, pp. 1470-1481, 2009.
- [95] M. Gruber, P. F. Joseph and M. Azarpeyvand, "An experimental investigation of novel trailing edge geometries on airfoil trailing edge noise reduction," in *19th AIAA/CEAS Aeroacoustics Conference*, Berlin, 2013.
- [96] M. Herr, "A noise reduction study on flow-permeable trailing-edges," in *8th ONERA-DLR Aerospace Symposium*, Göttingen, 2007.

- [97] E. J. Richards and D. J. Mead, *Noise and Acoustic Fatigue in Aeronautics*, London: John Wiley & Sons Ltd, 1968.
- [98] A. S. Hersh, P. T. Soderman and R. E. Hayden, "Investigation of acoustic effects of leading-edge serrations on airfoils," *Journal of Aircraft*, vol. 11, no. 1, pp. 197-202, 1974.

